



# Origin of Quasi-periodic Pulsation at the Base of a Kink-unstable Jet

Sudheer K. Mishra<sup>1</sup>, Kartika Sangal<sup>2</sup>, Pradeep Kayshap<sup>3</sup>, Petr Jelínek<sup>4</sup>, A. K. Srivastava<sup>2</sup>, and S. P. Rajaguru<sup>1</sup><sup>1</sup>Indian Institute of Astrophysics, Koramangala, Bangalore-560034, India<sup>2</sup>Department of Physics, Indian Institute of Technology (BHU), Varanasi-221005, India<sup>3</sup>VIT Bhopal University, Kothari Kalan, Sehore, Madhya-Pradesh 466114, India; [virat.com@gmail.com](mailto:virat.com@gmail.com)<sup>4</sup>University of South Bohemia, Faculty of Science, Department of Physics Branišovská 1760, CZ—370 05 České Budějovice, Czech Republic

Received 2022 September 15; revised 2022 December 21; accepted 2023 January 3; published 2023 March 13

## Abstract

We studied a blowout jet that occurred at the west limb of the Sun on 2014 August 29 using high-resolution imaging/spectroscopic observations provided by the Solar Dynamics Observatory/Atmospheric Imaging Assembly and the Interface Region Imaging Spectrograph. An inverse  $\gamma$ -shaped flux rope appeared before the jet—morphological indication of the onset of kink instability. The twisted field lines of the kink-unstable flux rope reconnected at its bright knot and launched the blowout jet at  $\approx 06:30:43$  UT with an average speed of  $234 \text{ km s}^{-1}$ . Just after the launch, the northern leg of the flux rope erupted completely. The time–distance diagrams show multiple spikes or bright dots, which is the result of periodic fluctuations, i.e., quasi-periodic fluctuations (QPPs). The wavelet analysis confirms that QPPs have a dominant period of  $\approx 3$  minutes. IRIS spectra (Si IV, C II, and Mg II) may also indicate the occurrence of magnetic reconnection through the existence of broad and complex profiles and bidirectional flows in the jet. Further, we found that line broadening is periodic with a period of  $\approx 3$  minutes, and plasma upflow always occurs when the line width is high, i.e., multiple reconnection may produce periodic line broadening. The emission measure (EM) curves also show the same period of  $\approx 3$  minutes in different temperature bins. The images and EM show that this jet spire is mainly cool (chromospheric/transition region) rather than hot (coronal) material. Further, line broadening, intensity, and EM curves have a period of  $\approx 3$  minutes, which strongly supports the fact that multiple magnetic reconnection triggers QPPs in the blowout jet.

*Unified Astronomy Thesaurus concepts:* Spectroscopy (1558); Solar transition region (1532); Solar magnetic reconnection (1504); Solar ultraviolet emission (1533)

*Supporting material:* animations

## 1. Introduction

Solar jets are an integral part of the solar atmosphere, and they are an important feature of the mass/energy cycle within the solar atmosphere. Solar jets occur everywhere in the solar atmosphere. The solar jets have been classified into different categories based on different criteria, namely, (1) based on morphology—standard jets and blowout jets (Moore et al. 2010, 2013); (2) based on the region of the solar atmosphere where they occur—active-region jets, coronal hole jets, quiet-Sun jets, network jets, umbral jets, penumbral jets, and polar jets (Srivastava & Murawski 2011; Kayshap et al. 2013a, 2013b, 2018; Tian et al. 2014; Tiwari et al. 2016; Mulay et al. 2017; Srivastava et al. 2018); and (3) based on the filter in which they are observed—e.g., H- $\alpha$  jet, extreme ultraviolet (EUV) jets, ultraviolet jet (UV) jets, X-ray jets, and radio jets (e.g., Shibata et al. 1992; Innes et al. 1997; Shibata et al. 2007; Zhang & Ji 2014; Filippov et al. 2015; Sterling et al. 2015; Ni et al. 2017; Shen et al. 2017; Zhang & Ni 2019). Solar surges are another category of solar jet-like features, and they are made of mainly cool plasma. Therefore, cool lines/filters (e.g., H $\alpha$ , Ca II H and K line, Mg II h and k lines, Si IV, IRIS/SJI 1400 Å, AIA 304 Å, and many more) are used to observe the solar surges (e.g., Sterling 2000; Tziotziou et al. 2005; Kayshap et al. 2021a). However, the surges can heat the plasma up to a transition region/coronal temperature and then they

rapidly cool down to chromospheric temperatures (Nóbrega-Siverio et al. 2016; Nóbrega-Siverio et al. 2017; Nóbrega-Siverio et al. 2018; De Pontieu et al. 2021). In addition, Young (2015) has added one more category to the solar jets, i.e., dark jets, which have no intensity enhancement, but the signature exists in the Doppler velocity.

The energy required to power the solar jets comes from the complex magnetic field through the most widely occurring process (i.e., magnetic reconnection) in the solar atmosphere. These solar jets are distributed all over the solar atmosphere as magnetic reconnection can occur anywhere within the solar atmosphere when the suitable physical conditions are pronounced. Widely, the bipolar magnetic field reconnects with the preexisting magnetic field, and produces the jets in the solar atmosphere (e.g., Yokoyama & Shibata 1995; Shimojo et al. 1996; Yokoyama & Shibata 1996; Shibata et al. 2007; Nishizuka et al. 2008; Raouafi et al. 2016). Moreno-Insertis & Galsgaard (2013) performed a detailed numerical simulation, based on the magnetic reconnection between an emerging bipolar magnetic field with the preexisting open coronal magnetic field, to understand the triggering mechanisms and dynamics of solar jets. Further, in another remarkable work, Sterling et al. (2015) have shown that mini-filaments can also trigger the solar jets, i.e., the eruption of the mini-filaments trigger the magnetic reconnection, which ultimately produces the solar jet. In this continuation, Wyper et al. (2017) proposed the universal magnetic breakout model to trigger the jet, i.e., magnetic reconnection takes place due to mini-filament eruption. However, it must be noted that this magnetic breakout model was already known and widely used in the



Original content from this work may be used under the terms of the [Creative Commons Attribution 4.0 licence](https://creativecommons.org/licenses/by/4.0/). Any further distribution of this work must maintain attribution to the author(s) and the title of the work, journal citation and DOI.

triggering of the large-scale eruptions, and Wyper et al. (2018) extended this model to the formation of solar jets. As per the magnetic breakout model, the magnetic reconnection takes place due to mini-filament eruption and it finally triggers the jet in the solar atmosphere. Hence, we can say that magnetic reconnection is an integral process of the formation of solar jets.

There are at least three different theoretical explanations for plasma acceleration from various numerical simulations. In the first type of acceleration mechanisms, the plasma is accelerated from the magnetic reconnection site by the slingshot effect along the newly reconnected magnetic field lines (Yokoyama & Shibata 1996; Moreno-Insertis et al. 2008; Nishizuka et al. 2008). The released energy from the magnetic reconnection can be deposited through various ways, e.g., adiabatic compression, Joule heating, accelerated particles, and shocks. Hence, this energy released from the magnetic reconnection can heat the plasma impulsively and the strong pressure and temperature gradient will develop there, which can induce the evaporation flows (Shimojo et al. 2001; Miyagoshi & Yokoyama 2003; Matsui et al. 2012). The evaporation flow is the second plasma acceleration mechanism for the solar jets, and it is induced by magnetic reconnection. The speed in this mechanism (i.e., evaporation flow) of the jet plasma is much slower than the speed of the plasma attained through the slingshot effect. When the twisted closed magnetic field lines reconnect with the untwisted open field lines then the twist will transfer to the newly reconnected magnetic field lines. And, the newly reconnected magnetic field lines will exhibit untwisting motions, which are the third type of acceleration mechanisms induced by magnetic reconnection. The models, which are based on this mechanism, are known as the untwisting models of the solar jets (e.g., Shibata & Uchida 1986; Schmieder et al. 1995; Canfield et al. 1996; Jibben & Canfield 2004; Kamio et al. 2010; Archontis & Hood 2013; Moreno-Insertis & Galsgaard 2013; Fang et al. 2014). The helical/rotational motions (i.e., an important feature of the solar jets) can be explained through these untwisting models of the solar jets. In addition, it can be noted that the helical/rotational motion is a main feature of cool emissions of the solar jets (e.g., Canfield et al. 1996; Harrison et al. 2001; Kamio et al. 2010; Hong et al. 2013). The blowout jet mainly emits at a cooler temperature and they always exhibit a strong rotation (e.g., Sterling et al. 2010; Moore et al. 2013).

The physical process used in the untwisting models (i.e., reconnection between the twisted magnetic field and open magnetic field lines) is not the only way to trigger the solar jets and their helical or rotating motions. Various types of magnetohydrodynamic (MHD) instabilities (e.g., Rayleigh–Taylor (RT), Kelvin–Helmholtz (KH), Ballooning mode, convective-driven instability, radiatively driven instability, heat-driven thermal instabilities, tearing mode, kink mode, sausage mode, helical/torsional mode, and current-sheet mode) are important physical processes that trigger the wide varieties of the solar phenomena, i.e., from small-scale events (e.g., solar jets) to large-scale eruptions (Mishra et al. 2018; Mishra & Srivastava 2019; Mishra et al. 2021). Kink instability is one of the prominent mechanisms to trigger the solar jets (see the review within Raouafi et al. 2016). The observational and theoretical studies suggest that the rotational/twisting motions of the solar jets are directly linked with the helical kink

instability (Shibata & Uchida 1986; Pariat et al. 2009; Liu et al. 2019; Zaqarashvili et al. 2021).

The embedded magnetic dipole is a key feature of the numerical simulations based on the kink instability. Generally, the MHD instabilities are associated with the embedded magnetic bipole in such numerical simulations, and the kink instability takes place when the threshold in energy or helicity or twist exceeds some critical values (e.g., Pariat et al. 2009). The kink instability may evolve in a flux rope if the azimuthal component of the magnetic field exceeds some critical threshold (Aschwanden 2004). Theoretical and observational studies suggest different threshold values of twist/helicity for the kink instability, namely  $2\pi$  (Kruskal & Kulsrud 1958),  $2.5\pi$  (Hood & Priest 1981),  $2.6\pi$  (e.g., Pariat et al. 2009, 2015), and 1.3 turns (Liu et al. 2019). Hence, we can say that the threshold value of the twist to trigger kink instability varies a lot, and it depends on the magnetic field conditions. Now, this kink instability forces a loss of the stability of the whole stable magnetic field configuration (i.e., the embedded magnetic flux in the uniform magnetic field; Pariat et al. 2009), and it leads to the magnetic reconnection that drives the helical solar jets (Pariat et al. 2015). However, such magnetic field configuration is not the only possibility for helical jets. The high-resolution observations show the existence of a twisted flux rope, and the reconnection within the twisted magnetic structure can also produce such helical jets (Raouafi et al. 2010; Liu et al. 2011; Kayshap et al. 2013a).

The solar jets may also be the source of MHD waves (Cirtain et al. 2007; Zhelyazkov 2012) and quasi-periodic pulsations (QPPs; e.g., Morton et al. 2012; Zhang & Ji 2014). QPPs are a phenomenon frequently associated with solar flares, and these QPPs in solar flares occur over a vast range of periods, i.e., from a fraction of a second to several minutes (e.g., Nakariakov et al. 2010, 2016; Kashapova et al. 2020). The different periods of QPPs may be related to the different physical processes in the solar atmosphere. Recently, Zimovets et al. (2021) reviewed the observational and theoretical aspects of the QPPs in solar and stellar flares, and they suggest more than 15 different mechanisms in support of the formation of QPPs in solar/stellar flares. All these physical mechanisms for QPPs are primarily associated with either MHD waves or quasi-periodic regimes of magnetic reconnection. We know that QPPs are very common phenomena associated with solar/stellar flares, while the observational detection of QPPs in solar jets is very rare. So far, there are only a few observational works that report the existence of the QPPs in solar jets (e.g., Morton et al. 2012; Zhang & Ji 2014). Similar to the QPPs in solar flares, it is reported that multiple magnetic reconnections can trigger the QPPs in blowout jets also (Morton et al. 2012). Here, we mention that QPPs are not well studied in solar jets as there are only a few reports of QPPs in solar jets so far. And, on top of this fact, we further say that solar jet, kink instability, and the formation of QPPs are not investigated as per the best of our knowledge.

In the present scientific work, we provide a systematic observational study of solar jets triggered due to the kink instability, and subsequent evolution of QPPs. The observations and data analysis are discussed in Section 2. In Section 3 we present the observational results related to the eruption of kink-unstable jets and QPPs. Finally, the discussion and conclusion are presented in Section 4.

## 2. Observations and Data Analysis

The Atmospheric Imaging Assembly (AIA) on board the Solar Dynamics Observatory (SDO) provides the full-disk images of the Sun in several filters (AIA 4500, AIA 1600, AIA 1700, AIA 304, AIA 171, AIA 211, AIA 131, and AIA 94 Å; Lemen et al. 2012). Some filters capture the emission from the extreme ultraviolet (EUV)/UV region, and one filter of AIA captures the emission from the visible wave band. Therefore these AIA filters capture the emission of the Sun from the top of the photosphere to the lower corona. The spatial resolution of the EUV wave band is  $1''.5$  with  $0''.6$  per pixel width and a cadence of 12 s (see Lemen et al. 2012 for more details). We use multiwavelength imaging observations obtained from AIA/SDO for this work. The jet was triggered around  $\sim 06:28$  UT on 2014 August 29 near the west limb of the Sun and the jet event ended at  $\sim 07:20$  UT.

The AIA images are used to understand the temporal evolution of this jet event. In addition to the temporal evolution, the AIA images can also be used to perform differential emission measures (DEMs). The DEM is a very useful parameter to understand the thermal nature of this jet event. To estimate the DEM, we used the method developed by Hannah & Kontar (2012). This method uses a regularized inversion technique to perform the DEM using the warm/hot EUV channel of AIA/SDO (94, 131, 171, 193, 211, and 335 Å). It is an automated method that uses the zeroth-order regularized inversion to return the DEM as a function of temperature. This regularized method provides a positive solution for the extracted DEM. We divide the temperature range between  $\log T = 5.0-7.5$  K, with 25 temperature bins and an interval of  $\log \Delta T = 0.1$  K.

In addition to the AIA imaging observations, we also use imaging (slit-jaw images, SJI) and simultaneous spectroscopic observations obtained from the Interface Region Imaging Spectrograph (IRIS). The IRIS telescope captures the emission from the lower solar atmosphere (chromosphere and transition region) using an SJI, and IRIS takes images in far-ultraviolet (FUV; 1331.56–1358.40 Å and 1390.00–1406.79 Å) and near-ultraviolet (NUV; 2782.56–2833.89 Å) wave bands. IRIS does not provide full-disk images, but rather it provides small field-of-view (FOV) images of the Sun in some filters, namely, the Mg II 2796.0 Å filter, Si IV 1400 Å filter, C II 1330 Å filter, and more filters (for more details see De Pontieu et al. 2014). The IRIS has observed this jet event only in the C II 1330 Å filter with the temporal cadence of 10 s, and the full field-of-view (FOV) of SJI is  $119'' \times 119''$ .

The IRIS also provides spectroscopic observations, and it observes some of the prominent spectral lines of the interface region, such as Mg II k 2796 Å, Mg II h 2803 Å, C II 1334.53 Å, C II 1335.66 Å, Si IV 1393.76 Å, and Si IV 1402.77 Å. IRIS has observed the spectra of this particular jet event with an eight-step coarse raster observation with a temporal cadence of 9.6 s. Hence, each raster file of this observation takes  $\sim 77$  s ( $8.0 \times 9.6 = 76.8$  s).

Lastly, we mention that we also utilized a wavelet analysis to diagnose the quasi-periodic behavior of various light curves extracted from this jet event. We adopt the method of Torrence & Compo (1998) for the wavelet analysis of the time series. We have applied the wavelet analysis on AIA 304, AIA 171, AIA 131, and AIA 211 Å filter observations. We computed the wavelet power, global power, and 95% significance levels using the method developed by Torrence & Compo (1998).

## 3. Observational Results

We used the high-resolution multiwavelength imaging and spectroscopic data of AIA and IRIS to study an eruptive jet on 2014 August 29. This jet was situated near the west limb, and the jet was initiated around 06:28 UT. Here, we describe the whole jet event in the following subsections.

### 3.1. Onset of the Kink Instability

We use a sequence of AIA 304 Å images to understand the spatio-temporal evolution of kink instability in a blowout jet (see Figure 1). The images of Figure 1 are plotted in the reverse intensity. The direction system is displayed in the panel (a) of Figure 1. This blowout jet starts to lift at  $\approx 06:28$  UT from an active region NOAA 12146. At  $t = 06:29:07$  UT, we see the inverse  $\gamma$ -shaped structure outlined by a white dashed line (panel (a) of Figure 1), which is a manifestation of the writhing motion near the base of the jet. This magnetized structure (i.e., inverse  $\gamma$ -shaped structure) is developing with time, i.e., it is expanding and rising (panels (b) and (c) of Figure 1; see also animation of the Figure A1). In the meantime, the inverse  $\gamma$ -shaped structure performs an counterclockwise twist (see the Figure A1 animation) and, as a result, it may become kink-unstable. The characteristic inverse  $\gamma$ -shaped evolves due to the conversion of the initial twist into the writhe (Török et al. 2010, 2014), and the inverse  $\gamma$ -shape-like structure is a morphological signature for the onset of the kink instability.

We see that the inverse  $\gamma$ -shaped structure is lifting and expanding with time (panels (b) and (c) of Figure 1). Now, at time  $t = 06:30:19$  UT, the inverse  $\gamma$ -shaped structure has fully developed, and again we outlined the fully developed structure by the white dashed line (panel (d) of Figure 1). We see little brightening around the knot (cross point) of the inverse  $\gamma$ -shaped structure. In addition, we also see localized bright dots, and two bright dots are indicated by two black arrows (see panel (d)). The bright dots further propagate upward along the magnetic field lines as the jet develops with time. The brightening at the knot (as indicated by white arrow in the panel (e) of Figure 1) is becoming stronger and wider with time (see panels (e) and (f) of Figure 1 as well as the Figure A1 animation).

Meanwhile, the plasma is moving up along the magnetic field forming the main body of this jet. This jet is not well collimated as the width of the jet is increasing with time (see panels (d), (e), (f), (g), (h), and (i) of Figure 1 as well as the Figure A1 animation). Hence, this jet is a typical blowout jet as per the morphological classification of the solar jets (e.g., Moore et al. 2010, 2013). The jet is made of various plasma threads, and out of them, we marked one plasma thread at 06:30:43 UT by a black arrow (panel (e) of Figure 1). This particular thread is located at the top edge of the jet this time (06:30:43 UT), and further, we traced this particular plasma thread at various other times (please see the black arrows from panel (e) to (l) of Figure 1). This particular thread follows a counterclockwise motion with time, which suggests that the jet spire is rotating. In addition, we have also shown the evolution of the jet using the IRIS 1330 Å filter (see Figure A1). This animated figure describes the main features of the jet as per the IRIS animation (Figure A1). Similar to AIA 304 Å, the IRIS/SJI 1330 Å filter observations also show the rotating motion of the jet. Hence, finally, we can say that the rotating motion of the jet plasma is also visible in the animation of Figure A1.

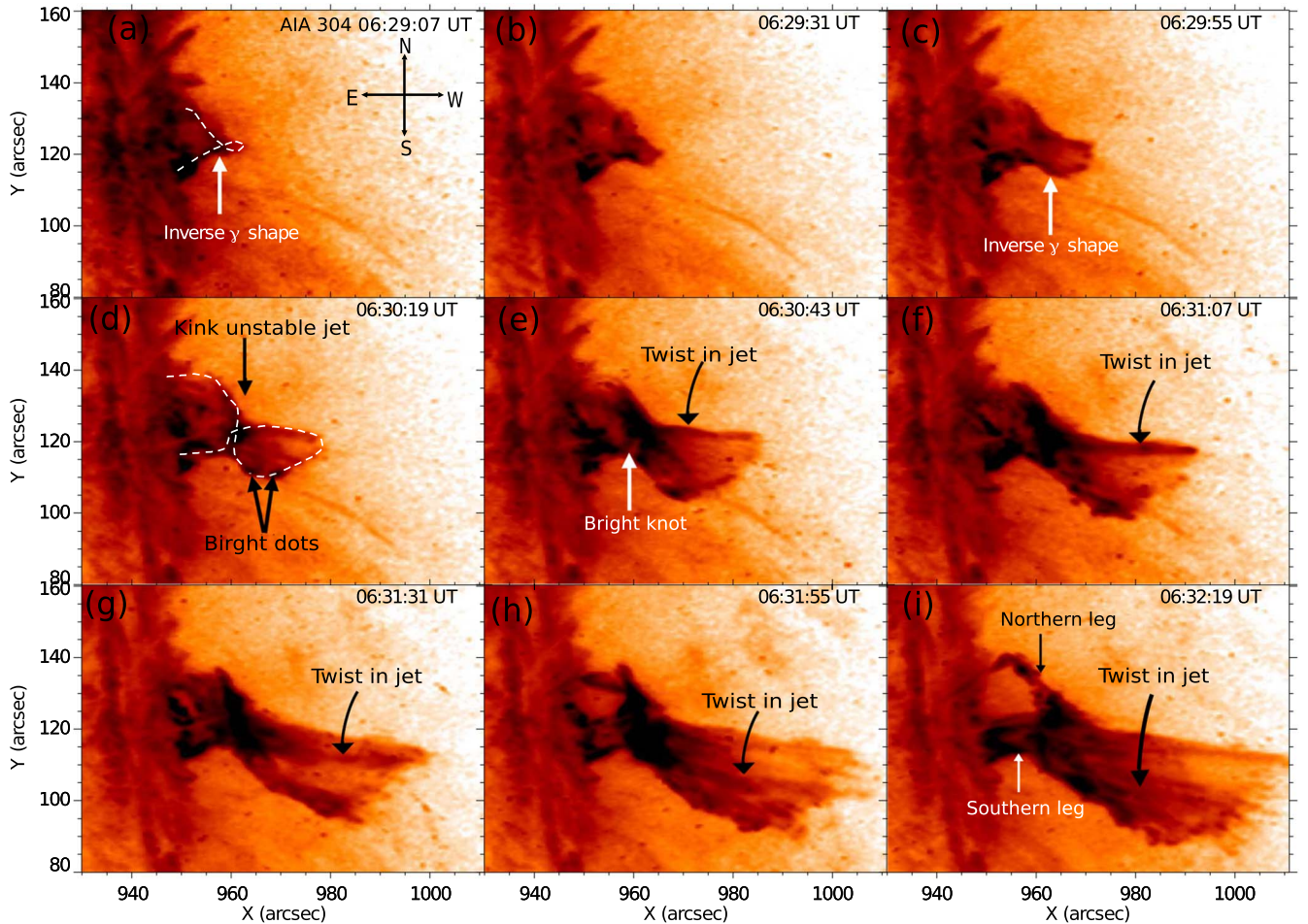


**Figure 1.** The sequence of the images from SDO/AIA 304 Å with reverse color contrast shows the onset of the kink instability in a blowout jet. The morphological sign of kink instability (inverse  $\gamma$ -shape), bright knot, propagation of brightening along the twisted field lines, and rotation of the plasma thread (i.e., twist in the jet) have been identified, and these observational findings are indicated by the different arrows. The first panel shows the direction to better understand the dynamics in the jet's leg. The black and white arrows indicate the northern and southern legs of the eruptive jet (last panel).

### 3.2. Multiwavelength Imaging Observations of the Solar Jet

In the previous subsection (Section 3.1) we described the dynamics of the inverse  $\gamma$ -shaped flux rope and the triggering of the blowout jet. In this subsection we are investigating the dynamics of the blowout jet in cool (AIA 1600, AIA 304, and IRIS/SJI 1330 Å) and warm/hot temperature filters (AIA 171, AIA 131, and AIA 94 Å) to understand the multiwavelength nature of this jet. The distinction between the hot and cool temperature filters is relative, and the classification between the hot and cool temperatures may change from case to case. Here, in the present study, we say that AIA 1600, AIA 304, and IRIS/SJI 1330 Å are cool filters while AIA 171, AIA 131, and AIA 94 Å are warm/hot filters. We know that this inverse  $\gamma$ -shaped magnetic structure lifts up with time (see Figure 1). Here, in this subsection, we discussed the multiwavelength observations of the blowout jet. Figure 2 shows the spatio-temporal evolution of the jet in the AIA 1600 Å (top row), IRIS/SJI 1330 Å (second row), AIA 171 Å (third row), and AIA 131 Å (fourth row) wave bands. Similar to Figure 1, we have again displayed the directions in panel (a1) of Figure 2. At  $t = 06:29:23$  UT, the inverse  $\gamma$ -shaped structure has significantly developed, and the top of this structure is well above the limb. This inverse

$\gamma$ -shaped structure is clearly visible in the cool temperature filters (panels (a1), (a2), (b1), and (b2) of Figure 2), but it is not visible in the hot temperature filters (panels (c1), (c2), (d1), and (d2) of Figure 2 and its animation). However, we see the brightened base of the inverse  $\gamma$ -shaped structure in the hot temperature filters.

At the next time ( $t = 06:29:30$  UT) we clearly see the jet in the cool temperature filter, indicated by the black arrows (see panels (a2) and (b2) of Figure 2). At this time, we see a compact brightening in the vicinity of the knot of the inverse  $\gamma$ -shaped structure (indicated by black arrows in panels (c2) and (d2) of Figure 2) in the hot temperature filters (panels (c2) and (d2) of Figure 2). We do not see the spire of the jet in the hot temperature filters as we have seen in the cool filters. At the next time ( $t = 06:31:18$  UT), the jet is fully developed with two legs rooted at the solar surface (panels (a3) and (b3) of Figure 2). The upper leg is denoted as the northern leg while the lower leg is denoted as the southern leg. And, these two legs are clearly indicated by the white and black arrows in panels (a3) and (b3) of Figure 2, respectively. Interestingly, we do see the signature of bidirectional flows, i.e., plasma falls along both legs below the bright knot (see the red arrows in panels (a3), (b3), (c3), and (d3) of Figure 2 and its animation) while the plasma flows up above the bright

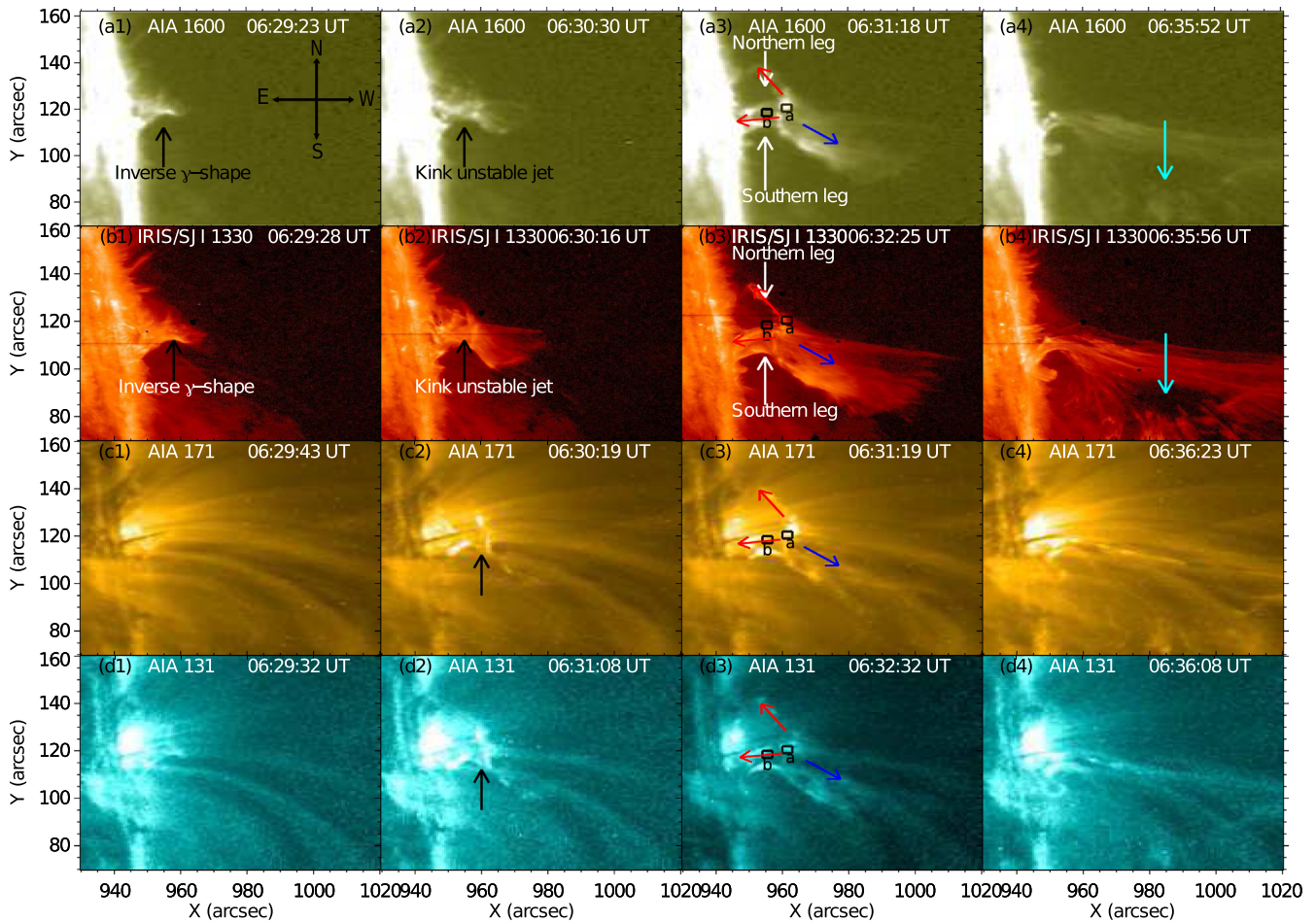


**Figure 2.** The figures show the multiwavelength view of the kink-unstable blowout jet observed on 2014 August 29 by SDO/AIA and IRIS. It shows the morphological evolution of the kink-unstable blowout jet in the different layers of the solar atmosphere (AIA 1600 (top row), IRIS/SJI 1330 (second row), AIA 304 (third row), and AIA 131 (bottom row)). In this evolution, we have seen various important features of this blowout jet, namely, the development of the inverse  $\gamma$ -shape in the cool filters (panels (a1) and (b1)), the bright knot due to magnetic reconnection along with the triggering of the blowout jet (panels (a2), (b2), (c2), and (d2)), the bidirectional flows from the bright knot (panels (a3), (b3), (c3), and (d3)), and the matured phase of the jet with a cavity (panels (a4) and (b4)). Here, it should be noted that the jet is mainly visible in the cool filters, and does not emit much in the hot filters. However, we see a compact bright structure in the hot filters (see panels (c2) and (d2)) which justifies the occurrence of internal magnetic reconnection in highly twisted magnetic field lines of the inverse  $\gamma$ -shape near its apex. The northern and southern legs are indicated by the white and black arrows in the panels (a3) and (b3). The two boxes “a” and “b” are shown in panels (a3), (b3), (c3), and (d3). We used these boxes to investigate the total EM (see Figures 4(c) and(d)). An animation of panels (c) and (d) is available. The animation also includes the AIA 304 and AIA 94 Å sequences. The animation shows the triggering and the complete evolution of the kink-unstable jet and their association with the multithermal plasma. The kink instability at the base of the jet, the triggering of magnetic reconnection, the eruption of the jet, and the associated dynamics are shown between 06:25 UT and 06:59 UT. The real-time duration is 13 s for this animation.

(An animation of this figure is available.)

knot (see the blue arrows in panels (a3), (b3), (c3), and (d3) of Figure 2). This bidirectional flow is also clearly visible in the animation. This up-and-downflow of the plasma builds the main body of this blowout jet. Also, the bidirectional flows of the jet are visible in the cool filters. However, we only see some faint signatures of the blowout jet in the hot temperature filters (panels (c3) and (d3) of Figure 2). At time  $t = 06:35:52$  UT the northern leg of inverse  $\gamma$ -shaped flux rope is completely disconnected from the solar limb while the southern leg remains connected to the limb of the Sun (panels (a4), (b4), (c4), and (d4) of Figure 2). Now, the jet is fully developed at this time along southern leg. Interestingly, we see a big cavity in the jet plasma that is indicated by the cyan arrows (panels (a4) and (b4) of Figure 2). It seems that some plasma from the main body of the jet has bifurcated, and the space between the main body and the bifurcated plasma of the jet appears in the black region (i.e., the cavity).

### 3.3. Time–distance Analysis of Blowout Jet

We performed the time–distance estimation along and across (perpendicular) the blowout jet to understand the kinematics of this blowout jet (see Figure 3). We displayed the late phase of the blowout jet along with one horizontal slit (S1) and four vertical slits (P1, P2, P3, and P4) in panel (a) of Figure 3. All of the slits are shown by white dashed lines (panel (a)). As we have already indicated that the jet is mainly visible in the cool temperature filters, the time–distance analysis is performed using the cool temperature filter, AIA 304 Å. Panel (b) of Figure 3 shows the time–distance diagram corresponding to the horizontal slit (S1). We considered a width of 30 pixels around the horizontal slit (i.e., 15 pixels on each side of the slit) for the time–distance diagram shown in panel (b) of Figure 3. We drew a path (dashed cyan line) on the ascending motion of the jet plasma, and it is found that the jet plasma is moving up with a speed of  $234.0 \text{ km s}^{-1}$ . Interestingly, on the close inspection,

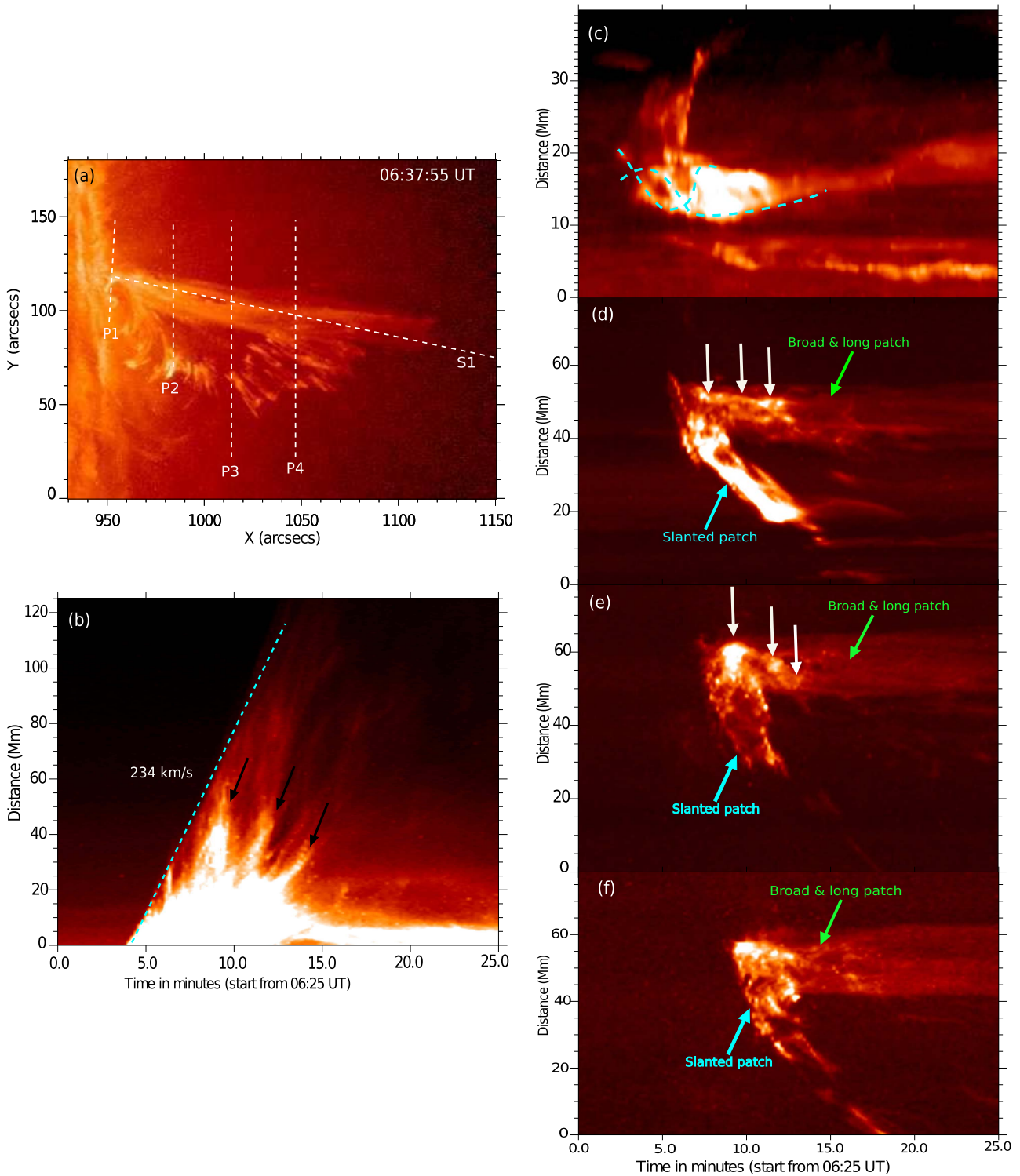


**Figure 3.** Panel (a) shows the intensity image from AIA 304 Å at  $t = 06:37:55$  UT, i.e., from the decay phase of the jet. The overplotted dashed lines are various slits along (S1) and across (P1, P2, P3, and P4) the jet, and they are used to produce the time–distance diagrams. The time–distance diagram along the S1 is shown in panel (b) and we drew a line (dashed cyan line) along the ascending phase of the jet to estimate the speed of the blowout jet, which is  $234 \text{ km s}^{-1}$ . We have also seen multiple spikes in this time–distance diagram which are indicated by the black arrows. In the right column, we have shown the time–distance diagrams along slits P1 (panel (c)), P2 (panel (d)), P3 (panel (e)), and P4 (panel (f)). Here, we have seen the opposite motion of the inverse  $\gamma$ -shape as indicated by the path drawn by the cyan dashed line in panel (c). Further, we have also seen the bright dot jet’s body which is indicated by the white arrows (panels (d) and (e)). Here, we see a slanted intensity patch (panels (d), (e), and (f)) in the last three panels of the right column which is occurring due to the fragmented plasma on a curved path from the main body of the blowout jet.

we noticed the multiple intensity enhancements at regular intervals as indicated by the black arrows in panel (b) of Figure 3. Here, we identified at least three peaks.

The right column of the Figure 3 shows four time–distance diagrams of the jet deduced from four different heights, i.e., along slits P1 (panel (c)), P2 (panel (d)), P3 (panel (e)), and P4

(panel (f)). Again, we used the same width of 30 pixels on both sides of all four slits (15 pixels on both sides of the slit) in the production of time–distance diagrams. Panel (c) shows the time–distance diagram along the first vertical slit P1. We have already shown the presence of an inverse  $\gamma$ -shaped flux rope, and the legs of this flux rope show opposite motion before the jet eruption (see Section 3.2). The slit P1 is located at the base of the jet and covers both legs of the inverse  $\gamma$ -shaped flux rope. We observe two opposite motions of the plasma (white dotted curve in panel (c) of Figure 3). This particular pattern is visible due to the opposite motion of the legs of the flux rope.

The time–distance diagram as per the second slit P2 is displayed in panel (d) of Figure 3. In the first instance, we see two different intensity patches in the time–distance diagram, i.e., the first one is a long and broad patch (indicated by the green arrow) while the second one is a narrow and slanted patch (indicated by the cyan arrow). In the very initial phase, the blowout jet had a single body, while after some time the jet body was bifurcated into two parts with a cavity in between them, as already explained in Section 3.2. Even in the reference image (panel (a) of Figure 3) one can see the long straight main body of the jet and some plasma fragments are distributed on a curved path below the main body of the jet. The base of slit P2 lies on the curved path, and then the slit crosses some part of the cavity before covering the main body of the jet. Hence, the bottom narrow, slanted intensity patch (indicated by the cyan arrow) in the time–distance diagram forms due to the plasma fragments along a curved path. While the long and broad patch (indicated by the green arrow) is due to the dynamics of the main jet body.

The main body of the blowout jet contains small bright dots that are indicated by the white arrows in the long, straight intensity patch. The time–distance diagram along the slit S1 (panel (b) of Figure 3) has already shown the multiple intensity peaks. We observe that the same intensity enhancement is visible as the multiple bright dots on regular time intervals in this time–distance diagram (panel (d) of Figure 3) drawn for the across the jet (i.e., slit P2). Here, at least we identified three bright dots, and it should be noted that these bright dots are aligned on the slanted path in the broad and long patch.

The time–distance diagram corresponding to slit P3 is displayed in panel (e) of Figure 3. Similar to the previous time–distance diagram, at this height we also see the bright dots in the main body of the jet. Here again these bright dots are indicated by the white arrows in the time–distance diagram corresponding to slit P3 (panel (e) of Figure 3), and these bright dots are on the slanted path in the long and broad patch (indicated by the green arrow). The narrow, slanted patch of intensity (indicated by the cyan arrow) exists here as already seen in panel (d) of Figure 3. The last vertical slit (slit P4) is located very far away from the base of the jet and panel (f) of Figure 3 shows the time–distance diagram corresponding to this slit. Again, we see both patches of intensity as already seen in panels (d) and (e), although, intensity in the slanted patch is weak in comparison to panels (d) and (e) of Figure 3. It is because slit P4 is located near the top part of the jet. However, we see the multiple bright dots like the time–distance diagrams corresponding to the slits P2 (panel (d)) and P3 (panel (e)) of Figure 3.

### 3.4. Thermal Structure of the Blowout Jet

We perform the DEM analysis to understand the thermal nature of this blowout jet. We use the regularized inversion code developed by Hannah & Kontar (2012) to extract the DEM using hot AIA/SDO filters. We use six hot, optically thin EUV filters (94, 131, 171, 193, 211, and 335 Å) of the AIA/SDO to estimate the DEM coming from different temperatures bins. In panels (a1), (a2), and (a3) of Figure 4 we displayed three emission measure (EM) maps deduced from three different temperature ranges ( $\log T/K = 5.7\text{--}6.0$ ,  $\log T/K = 6.0\text{--}6.3$ , and  $\log T/K = 6.9\text{--}7.2$ ) during the onset of the kink instability ( $t = \sim 06:32:03$  UT). Similarly, in panels (b1), (b2), and (b3) of Figure 4, we have shown the same three EM maps during the developed phase of the blowout jet ( $t = \sim 06:35:03$  UT).

In the initial phase, the EM maps show significant emission around the bright knot (as defined previously in Sections 3.1 and 3.2) above the legs of the inverse  $\gamma$ -shaped flux rope as indicated by the black arrows in panels (a1), (a2), and (a3) of Figure 4. The emission in the bright knot region exists over a very wide range of the temperature,  $\log T = 5.7$  to 7.2 K. Hence it justifies the presence of multithermal plasma at the knot of the inverse  $\gamma$ -shaped flux rope. After approximately 3 minutes, the emissions in the vicinity of the bright knot are significantly reduced (see panels (b1), (b2), and (b3) of Figure 4), although we see little emission in the bottom region of the bright knot and a faint jet originating from this little emission area. The faint jet is indicated by the black arrows in panels (b1), (b2), and (b3) of Figure 4. This EM study indicates that the spire of the jet has very little hot emission. That is consistent with this jet showing up strongly in the cool filters and being very faint in the hot filters.

We selected box (a) within the bright knot region (see the black rectangular box in panel (a1) of Figure 4) to know the temporal behavior of the DEM. We classify the entire DEM into five different temperature ranges (bins), namely, 0.5–1.0, 1.0–2.0, 2.0–4.0, 4.0–8.0, and 8.0–15 MK. Then, we estimated the emission ( $EM = \int_{T_{\min}}^{T_{\max}} DEM(T) dT$ ) in all of the above specified temperature bins. Through this approach, we got five different EM curves and they are displayed by five different colors in panel (c) of Figure 4. It is visible that all five curves show a dominant peak during the formation of the bright knot. The total emission in all of the five temperature ranges is highest during the formation of the bright knot.

We also extracted the EM curves from another box (box (b)), which is situated inside the southern leg of the blowout jet (please see box (b) in panel (b1) of Figure 4). These EM curves are displayed in panel (d) of Figure 4. Interestingly, the EM curves from box (b) show a periodic nature, unlike the nature of the EM curves deduced from box (a) (panel (c) of Figure 4). Box (a) is located in the northern leg of the blowout jet that erupts completely during the initial phase of the blowout jet. The plasma is completely swept away in the vicinity of the northern leg right after its eruption. Hence, we see only one dominant peak in the EM curves extracted from the box (a), while box (b) is situated near the base of the stable leg (southern leg) of this blowout jet. The periodic nature of the EM curves extracted from box (b) is present in all five of the temperature bins. We can easily locate at least three to four peaks in each EM curve, and it matches the intensity light curves extracted from the different boxes from cool

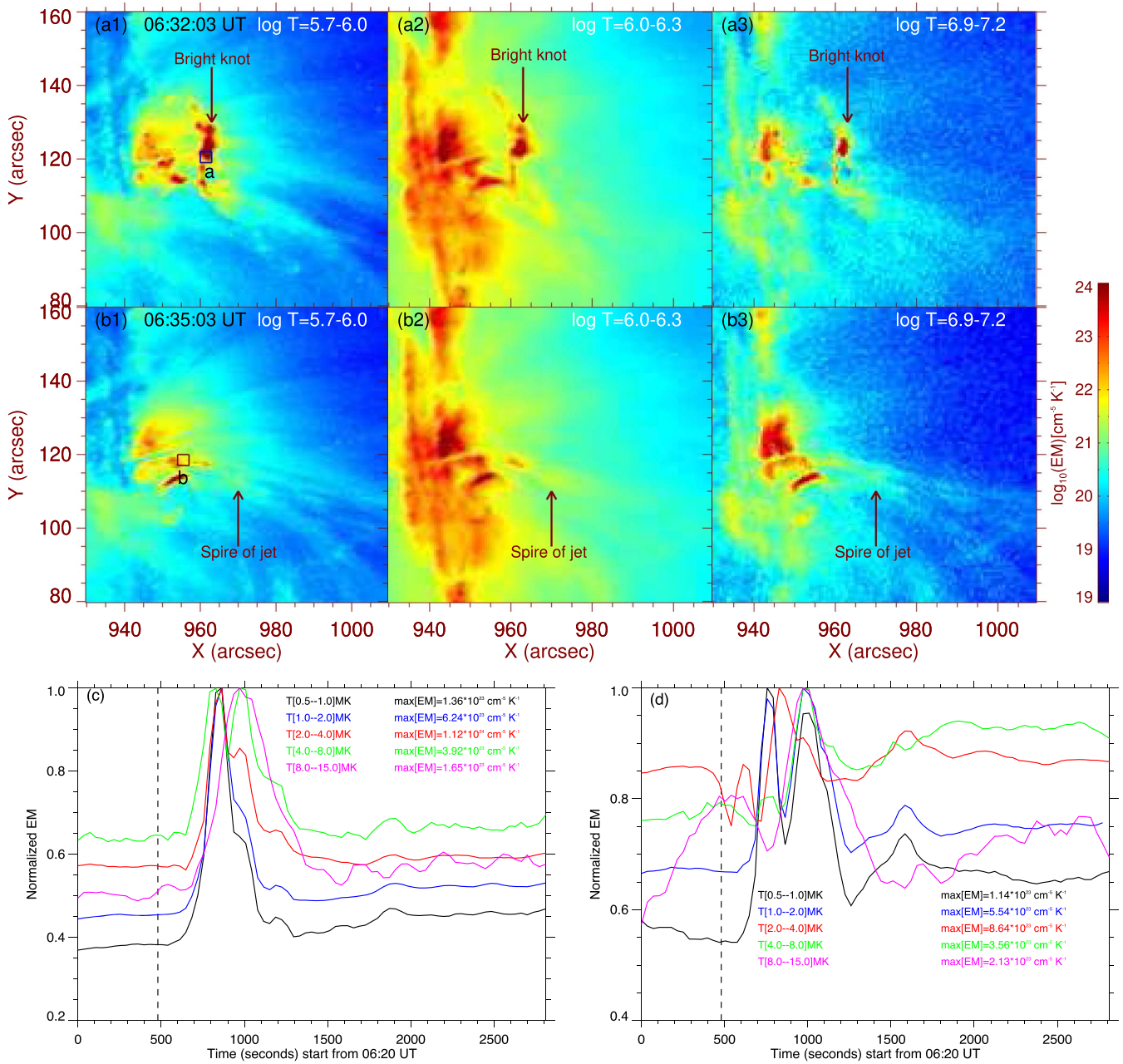


**Figure 4.** Panels (a1), (a2), and (a3) show the EM maps in three different temperature ranges ( $\log T/K = 5.7-6.0$ ,  $6.0-6.3$ , and  $6.9-7.2$ ) during the time  $t = 06:32:03$  UT when the magnetic reconnection takes place around the bright knot of the inverse- $\gamma$  structure. The bright knot is indicated by the black arrows in all of the panels in the top row. Similarly, the middle row shows the same EM maps during the developed phase of this blowout jet ( $t = 06:35:03$  UT). Here we see very faint emission of the jet as indicated by the black arrows in the middle row. Further, we selected one box in the northern leg (box (a)) and another box in the southern leg (box (b)) to investigate the temporal variations of the EM curves in various temperature ranges. Various EM curves are shown in panels c (box a) and d (box b) of Figure 4 by various colors. The color scheme and temperature ranges are mentioned in both panels. All EM curves from box (a) show only one peak while all EM curves from box (b) show three to four peaks. Box (a) is located in the northern leg which erupts in the initial phase of the jet.

temperature filter AIA 304 Å (see Section 3.6). The vertical black dotted line in the lower panels (panels (c) and (d) of Figure 4) indicates the jet event start time ( $t = \sim 06:28$  UT).

### 3.5. Spectroscopic Diagnosis of the Blowout Jet

In addition to the slit-jaw images, IRIS has also captured the NUV as well as FUV spectra of this jet event. Panel (a) of Figure 5 shows the IRIS/SJI intensity map at a time of  $\sim 06:32:06$  UT. IRIS observed the event with a roll angle of  $90^\circ$ . Therefore, this IRIS/SJI intensity map (panel (a) of Figure 5) is  $90^\circ$  rotated in comparison to other figures

(Figures 1, 2, and 3) in this manuscript. Here we mention that the directional system is added in panel (a) of Figure 5. We overplotted all eight slit positions (eight vertical gray dashed lines) on this IRIS/SJI intensity map (panel a). Then we chose two locations to know the nature of the Si IV, C II and Mg II profiles, namely, the red plus sign ( $x = 993''12$  and  $y = 95''19$ ) and the blue plus sign ( $x = 997''12$  and  $y = 93''52$ ). It should be noted that the selected locations (the red and blue plus sign in panel (a) of Figure 5) are located in the vicinity of the bright knot region, i.e., most probably in the magnetic reconnection region.

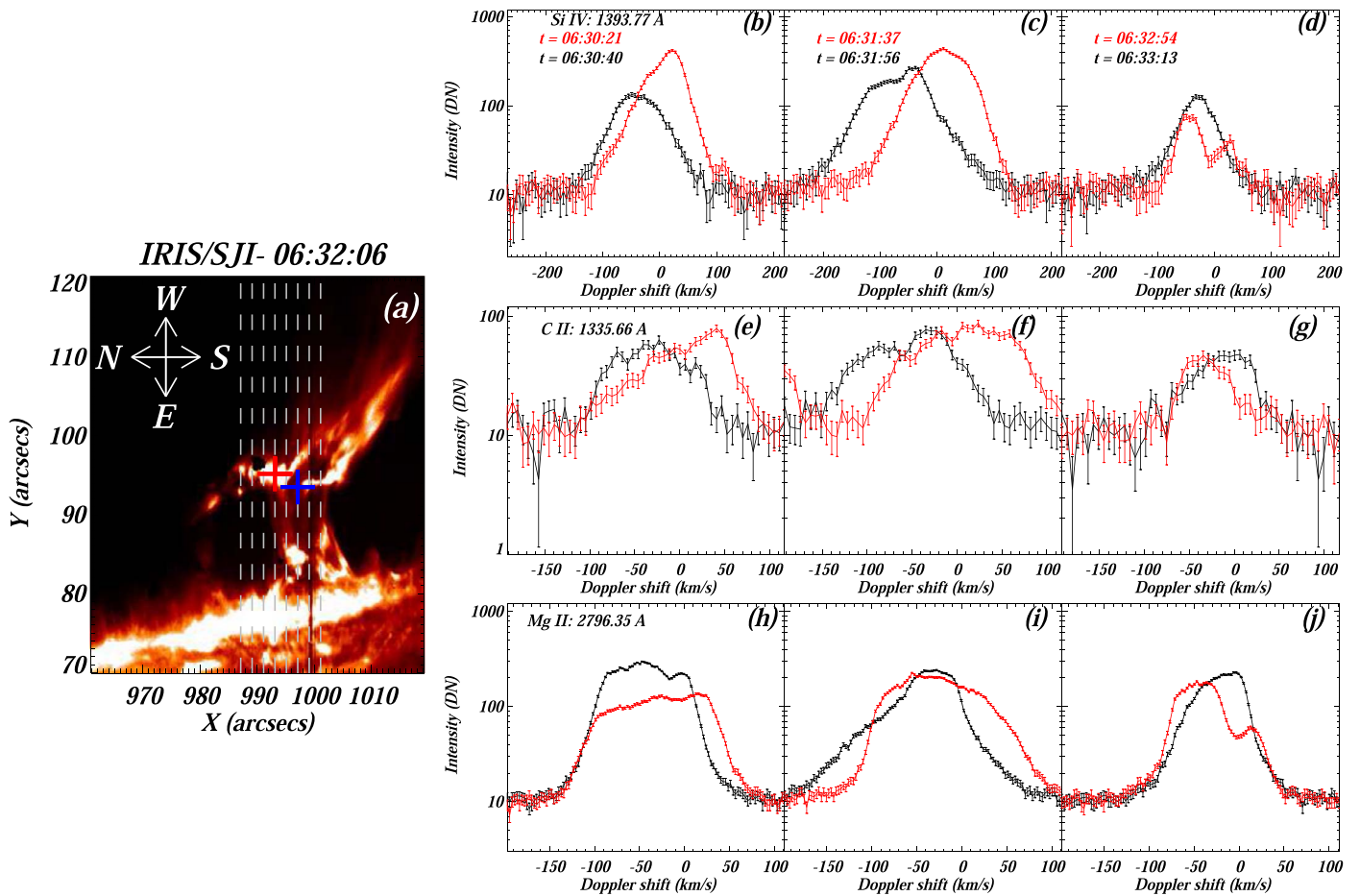


**Figure 5.** The IRIS/SJI 1330 Å image depicts the blowout jet at time  $t = 06:32:06$  UT along with eight slit positions shown by the white dashed lines in panel (a). IRIS captured the spectra along these slits. Further, we selected one location (red plus sign) in the northern leg with another location (blue plus sign) in the southern leg of the blowout jet. Panels (b), (c), and (d) show the spectral profiles of Si IV from both locations (the red curve from red plus sign location and the black curve from blue plus sign location) at times of  $t = 06:30$  UT (panel (b)),  $06:31$  UT (panel (c)), and  $06:32$  UT (panel (d)). In the same fashion, we show C II (panels (e), (f), and (g)) and Mg II (panels (h), (i), and (j)) from both locations at the same three times. In general, all of the spectral profiles from the red plus sign location are redshifted (i.e., plasma downfall) while these profiles are blueshifted (i.e., plasma upflows) from the blue plus sign location. In addition, all of the spectral profiles are very complex.

In the imaging analysis, we have already shown the existence of the bidirectional flows in this jet event (see Section 3.2). And, as per the imaging analysis, the red plus sign lies in the downflow region while the blue plus sign is in the upflow region (see Figure 2 and Section 3.2). In Figure 5 we display the Si IV 1393.77 Å spectral profiles from red plus sign location by the red curve at three different times ( $06:30:21$  UT (panel (b)),  $06:31:37$  UT (panel (c)), and  $06:32:54$  UT (panel (d))). Similarly, the Si IV 1393.77 Å spectral profiles from blue plus sign locations are displayed by the black curve at three different times ( $t = 06:30:40$  UT (panel (b)),  $06:31:56$  UT (panel (c)), and  $06:33:13$  UT (panel (d))). In the same way, we have shown the spectral profiles from the red plus sign (red curve) and blue plus sign locations (black curve) of the C II 1335.66 Å spectral profiles (see panels (e), (f), and (g)) and Mg II 2796.35 Å (see panels (h), (i), and (j)).

We noticed that all black profiles (from Si IV, C II, and Mg II at all three times) are blueshifted (upflows) while all the red profiles are redshifted (downflows). Hence, we can say that all three spectral lines (Si IV, C II, and Mg II) justify that the red plus sign location is dominated by plasma downfall while the blue plus sign location is dominated by upflows, i.e., the spectra confirm the presence of bidirectional flows in the

vicinity of the bright knot. Hence, finally, we can say that both (spectra and images) confirm the presence of bidirectional flows in the vicinity of the bright knot. In addition, we do see very broad profiles from the Si IV, C II, and Mg II spectral lines during the initial/main phases of the blowout jet. The Si IV 1393.77 Å spectral line is an optically thin line and normally it has a single peak. However in this blowout jet the Si IV 1393.77 Å spectral line is either double peaked or has a highly asymmetric profile (panels (b), (c), and (d) of Figure 5). On the other hand, the C II 1335.62 Å and Mg II 2796.35 Å spectral lines are optically thick lines, and mostly, they appear as double peak profiles in the solar atmosphere. However, in this blowout jet, we see the very complex type of profiles from C II 1335.62 Å (see panels (e), (f), and (g)) and Mg II 2796.35 Å (see panels (h), (i), and (j)). Such types of complex profiles are reported in some small-scale energetic events (e.g., Peter et al. 2014; Young et al. 2018).

Further, we took five pixels around the blue plus sign location (see panel (a) of Figure 5) and then all five profiles were averaged to get a single averaged Si IV profile at any particular instant of time. Through this approach, we have produced 33 averaged spectral profiles in a time range from  $06:21:43$  UT to  $07:06:25$  UT. This observation is an eight-step

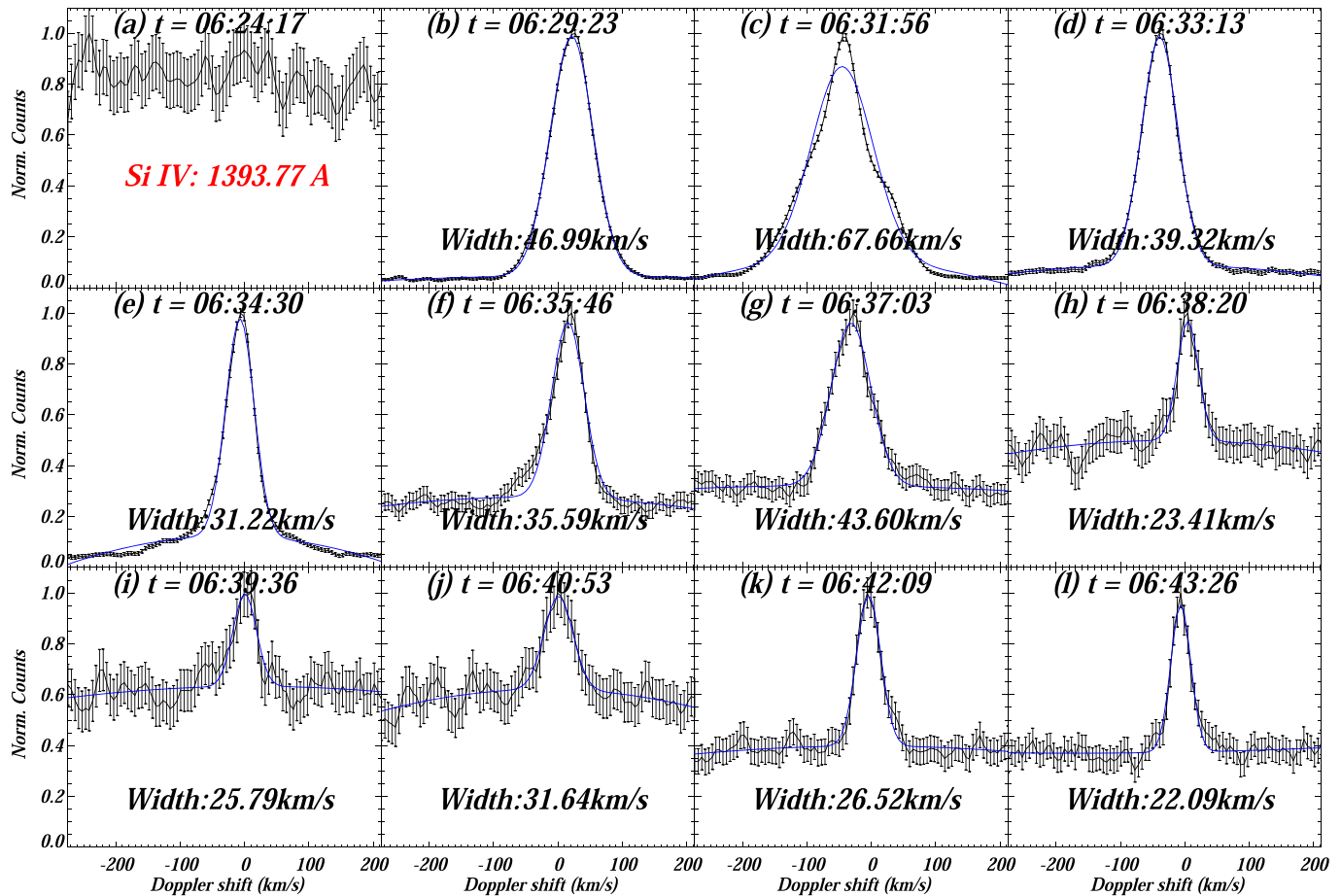


**Figure 6.** The temporal evolution of the normalized averaged Si-IV line profiles (averaged over the five pixels around the blue plus sign location shown in Figure 5) from the most probable reconnection region. It should be noted that all of the spectral profiles are normalized by their maximum counts and all the spectral profiles are fitted by a single Gaussian (see the blue curve in all of the panels). We do see periodic fluctuations in the line width of Si IV. The first panel does not show the line as it is before the triggering of the solar jets.

coarse raster observation with the cadence of 77 s. Therefore, the averaged spectral profile of any location is available after every 77 s (i.e.,  $8.0 \times$  cadence time).

Some key averaged spectral profiles are displayed in Figure 6. Panel (a) does not show the presence of the Si IV line as it is well before the jet event ( $t = 06:24:17$  UT). While at  $t = 06:29:23$  UT we see the Si IV spectral line as the formation of the jet has already begun (see panel (b) of Figure 6). We fitted the line profile with the single Gaussian (blue curve) to estimate the peak intensity, Doppler velocity, and line width of the profile. The line width of this profile is high ( $46.99 \text{ km s}^{-1}$ ) at  $t = 06:29:23$  UT (panel (b)). At the next time  $t = 06:31:56$  UT, we found that the profile is very wide and asymmetric too. We fitted this profile with the single Gaussian and found a very high line width (i.e.,  $67.66 \text{ km s}^{-1}$ ). It should be noted that the line width has increased a lot (i.e.,  $67.66 \text{ km s}^{-1}$ ) in comparison to the previous time  $t = 06:29:23$  UT (panel (b)). After  $t = 06:31:56$  UT, we notice a decreasing pattern in the line width of Si IV 1393.77 Å profiles, i.e., the line width is  $39.32 \text{ km s}^{-1}$  at time  $t = 06:33:13$  (panel (d) of Figure 6) and  $31.22 \text{ km s}^{-1}$  at time  $t = 06:34:30$  UT (panel (e) of Figure 6). Hence, for approximately 3 minutes (from  $06:31:56$  UT to  $06:34:40$  UT) the line width shows a decreasing pattern as the line width falls from  $67.66 \text{ km s}^{-1}$  to  $31.22 \text{ km s}^{-1}$ .

However, this decreasing pattern in the line width breaks at  $t = 06:35:46$  UT as we see that the line width is now increasing with time (see panels (f) and (g) of Figure 6). But again, the line width decreases with time  $t = 06:38:20$  UT (panel (h) of Figure 6). And one more time (i.e., third time), we see the same behavior of the line width, i.e., the line width increases (panels (i) and (j) of Figure 6) and decreases further with time (panels (k) and (l) of Figure 6). This particular finding indicates that the line width of the Si IV spectral line has a periodic behavior.

To understand the periodic behavior of line width clearly, we plotted the line width with time (see panel (a) of Figure 7). As we know already, in the specified time range ( $t = 06:21:28$  UT to  $07:03:52$  UT) there are 33 spectral lines, i.e., 33 line widths values. The specified time range starts from  $06:21:28$  UT, however the jet appears in the selected region around  $06:28:07$  UT (see the dashed green vertical line in panel (a) of Figure 7). We know that there is no spectral line before  $06:28:07$  UT, therefore, all the points before the green dashed vertical line have zero line width. We see the increase and decrease in the line width on a regular interval of time (see panel (a) of Figure 7). The oscillating behavior of the line width exists up to the time of  $t = 06:48$  UT, i.e., up to the red dashed vertical line. After  $\sim 06:48$  UT the downfall phase of the blowout jet dominates, and we do not see much variation in the line width. So, finally, we can say that oscillations in the line width are present during the upflow phase of the blowout jet.

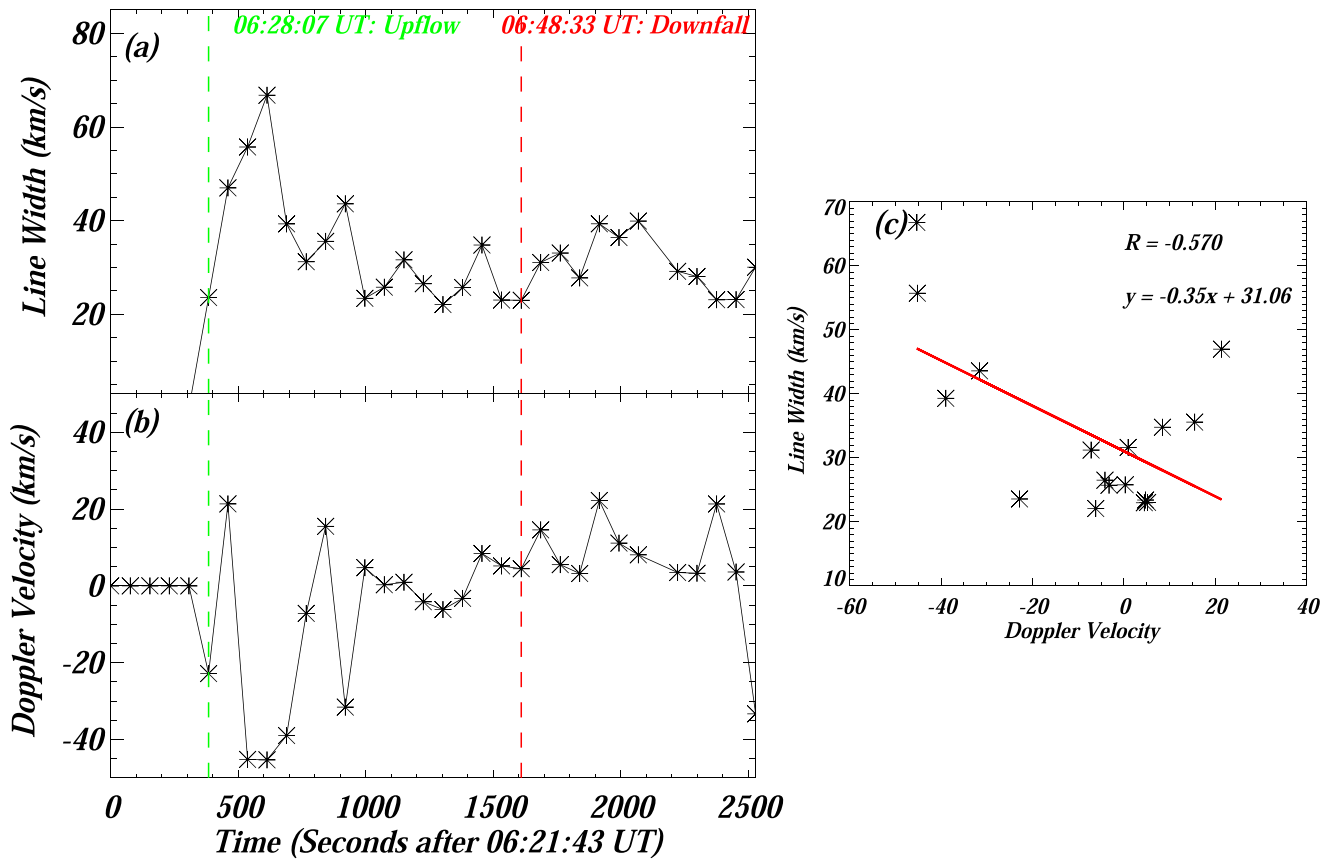


**Figure 7.** The temporal evolution of the line width and Doppler velocity from the most probable reconnection region (blue plus sign in Figure 5) is displayed in panels (a) and (b), respectively. The triggering time of the jet is indicated by the green dashed line; therefore, all the points before the green dashed line are zero. The downfall phase of the blowout jet dominates after the red vertical dashed line. In the upflow phase of the jet, we do see the periodic behavior of the line width. Further, we also see the periodic behavior of the Doppler velocity in the upflow phase of the blowout jet (panel (b)). We performed a correlation between the line width and the Doppler velocity which is shown in panel (c). It is found that line width is negatively correlated with the Doppler velocity, i.e., the line width is during the upflow, and the line width decreases as line profiles move toward the redshifts.

In addition to the line width, we have also shown the Doppler velocity with the time in panel (b) of Figure 7. The first few points are at zero Doppler velocity (up to the green dashed line) as the jet was not triggered by that time, and after that we do see the fluctuation in the Doppler velocities (see the points after the green dashed line). The careful inspection reveals that Doppler velocity is anticorrelated with line width during the upflow phase of the jet (i.e., points in between the green and red dashed lines). It means that when the line width is high, then Si IV line is blueshifted and vice versa. As the line width decreases with time, then in response, the Si IV line moves toward the redshifts. We have already pointed out that there are a few cycles of periodic increase and decrease in the line width during the upflow phase of the blowout jet. Similarly, we do see a kind of periodic behavior of the Doppler velocity too. After 06:48:33 UT, all spectral profiles are redshifted (see the points after the red dashed vertical line) as this is the downfall-dominant phase of the blowout jet. Further, we checked the correlation between the line width and Doppler velocity for the upflow-dominated phase of the blowout jet (i.e., points between the green and red dashed vertical lines), which is shown in the panel (c) of Figure 7. Now, it is clear that the line width and Doppler velocity are anticorrelated, i.e., the blueshifts (upflows) have high line widths, and when line width moves toward the redshifts (downflows) the line widths decrease. The Pearson coefficient is quite good (i.e.,  $-0.57$ ) for this correlation. Hence, we can

say that Doppler velocity and line widths are anticorrelated during the upflow phase of the jet.

### 3.6. Quasi-periodic Pulsation

We found the presence of QPPs during the blowout jet. We utilized the AIA 304, AIA 171, AIA 131, and AIA 211 Å filters to study the QPPs in this blowout jet. We selected four different boxes (B1, B2, B3, and B4) that are shown in the panel (a) of Figure 8 by different colors. Further, we estimated the averaged intensity curve (i.e., averaged over all of the pixels in the box) from all four boxes in all of the AIA filters (AIA 304, AIA 171, AIA 131, and AIA 211 Å). Panels (b) to (q) of Figure 8 show the wavelet analysis from four boxes. The wavelet analysis was performed on the averaged intensity light curves deduced from AIA 304 Å. Panel (b) of Figure 8 shows the averaged AIA 304 Å intensity curve (black curve) deduced from box (B1; black box in panel (a) of Figure 8). There is an overplotted red curve that is a smoothed, averaged intensity curve with a window of 15 points. Further, panel (f) shows the detrended intensity curve, i.e., averaged AIA 304 Å light curve (black curve) and the smoothed AIA 304 Å curve (red curve; panel (b) of Figure 8). Then we applied the wavelet analysis on this detrended light curve and the deduced wavelet power map is shown in panel (j) of Figure 8. Here we do see a concentrated patch of power around the period of 3 minutes (i.e., 3.03 minutes) for a time range from 6 to 20 minutes. Further, we

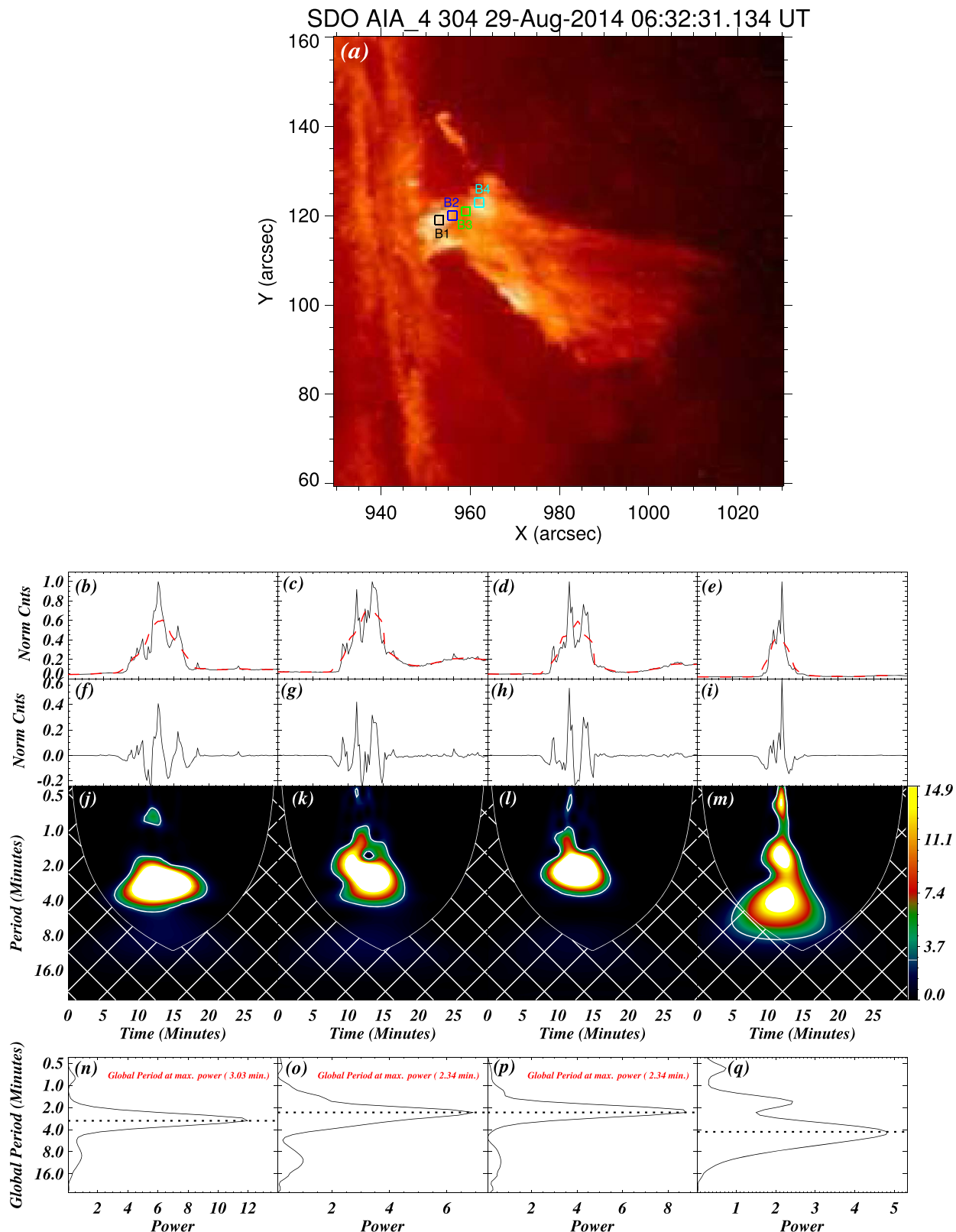


**Figure 8.** Panel (a) displays the SDO/AIA 304 Å image of the blowout jet at a time of  $t = 06:32:31$  UT and we select five boxes (B1, B2, B3, and B4) to deduce the emission curve from this filter. The temporal evolution of the intensity (i.e., black curve) in the AIA 304 Å filter from box (B1) is displayed in the first panel of the first column. The overlapped red dashed line is a smoothed curve with a window of 15 points. The second panel of the first column shows the detrended curve, and the wavelet transform is applied to this detrended curve. The wavelet power map is displayed in the third panel with 95% significance (i.e., white contours). The power is mainly concentrated around  $\sim 3$  minutes. Finally, in the last panel of first column, the global wavelet power is displayed which again shows that global power peaks around  $\sim 3$  minutes (i.e., 2.78 minutes). A similar analysis is shown for B2 (second column), B3 (third column), and B4 (fourth column), and the dominant period is  $\sim 3$  minutes. We did not find any significant period in B4.

estimated a 95% significance level, which is important to check the reliability of any detected period in the wavelet analysis, and the 95% significance level is shown by a white contour on the wavelet power map. Now it is visible that a concentrated patch of the power lies within the 95% significance level contours. The cross-hatched gray area in panel (j) of Figure 8 outlines the cone of influence (COI), and the powers inside this cross-hatched area are not reliable. But, here we can see that all of the significant powers are outside of the COI. In panel (n) of Figure 8, we show the global power (i.e., wavelet power averaged over time) against the period. The global power shows a dominant peak at a period of  $\sim 3$  minutes, i.e., 3.03 minutes.

We applied the wavelet analysis in the same fashion to all of the other boxes (i.e., B2, B3, and B4) which are shown in panel (a) of Figure 8. The original and smoothed intensity curves, detrended intensity curve, wavelet power maps, and global power maps are shown in the same manner for box B2 (panels (c), (g), (k), and (o)), box B3 (panels (d), (h), (l), and (p)), and box B4 (panels (e), (i), (m), and (q)) in the Figure 8. Boxes B2 and B3 show very similar behavior as to what we found for box B1. The dominant period is also approximately 3 minutes (i.e., 2.34 minutes for box B2 (panel (o) of Figure 8) and box B3 (panel (p) of Figure 8)) for almost the same time range from 6 to 20 minutes.

However, the intensity curve of the last box (i.e., B4) shows a sharp jump in the intensity for a short interval of time (i.e., around 5 minutes only). It is unlike to the other boxes (B1, B2, and B3) as fluctuations sustain a bit longer therein (around 15 minutes). We applied a wavelet analysis in the same manner as to that in box B4 and we found three concentrated patches of the power around the period of 6, 3, and 0.5 minutes (panel (q) of Figure 8). The wavelet power patches around the period of 6, 3, and 0.5 minutes persist only for 10 minutes, 5 minutes, and less than 1 minute, respectively. Hence, these periods of box B4 (i.e., 6, 3, and 0.5 minutes; panel (q) of Figure 8) do not even complete two cycles, therefore, we assume them as nonreliable power. In addition, some part of the longer period (6 minutes) also lies within the COI (panel (m) of Figure 8). Hence, finally, we can say that none of the power patches in the wavelet power map of box B4 is reliable, and we mention that B4 does not have any periodicity unlike the other boxes (i.e., B1, B2, and B3). We have also shown the QPPs in the same fashion for AIA 171 Å (see Figure B1), AIA 131 Å (see Figure B2), and AIA 211 Å (see Figure B3) in Appendix B. The findings from these fitters are similar to what we reported for AIA 304 Å here.

#### 4. Discussion and Conclusions

The present work provides an observation of the formation of blowout jet through kink instability. Initially, an inverse  $\gamma$ -shaped flux rope appeared on the west limb on 2014 August 29 that is a morphological indication for the onset of kink instability (Török & Kliem 2005; Pariat et al. 2009; Kayshap et al. 2013a; Hassanin & Kliem 2016). The inverse  $\gamma$ -shaped flux rope activates around 06:28:00 UT, i.e., this structure rises and expands with time. The twisted field lines are associated with the inverse  $\gamma$ -shaped flux rope, and these magnetic field lines reconnect. The primary magnetic reconnection took place around 06:31:00 UT near the apex of the inverse  $\gamma$ -shaped flux rope, i.e., in the vicinity of the bright knot. We witnessed the bidirectional flows from the apex of the flux rope through the

imaging analysis (Section 3.2). Various spectral lines (Si IV, C II, and Mg II) clearly show redshifted profiles (plasma downfall) below the apex, and all these profiles become blueshifted (plasma upflow) above the apex of the flux rope (see Figure 5), i.e., bidirectional flows. Hence, both (images and spectra) confirm the presence of bidirectional flows which is a typical characteristic of the magnetic reconnection in the solar atmosphere (Innes et al. 1997; Huang et al. 2014; Innes et al. 2015; Chitta & Lazarian 2020; Yang et al. 2020; Bahauddin et al. 2021; Antolin et al. 2021; De Pontieu et al. 2021). Further, DEM analysis shows the presence of multi-thermal plasma around the knot of inverse  $\gamma$ -shaped flux rope in the wide temperature range ( $\log T/K = 5.4\text{--}7.2$ ; Figure 4). Hence, these observational findings (bidirectional flows and multithermal plasma) indicate that the magnetic reconnection (primary) takes place around the knot of inverse  $\gamma$ -shaped flux rope that triggers the jet.

Soon after the primary magnetic reconnection, the northern leg of the inverse  $\gamma$ -shaped flux rope completely erupts, and further, the jet has developed only along the southern leg. Interestingly, we saw multiple bright regions (with time) within the jet. Here, we see multiple bright spikes in the time–distance diagram estimated per slit (i.e., S1) along the blowout jet. Similarly, the time–distance diagrams estimated per the slits (P2, P3, and P3) across the blowout jet show multiple bright dots (see Section 3.3). It is trivial to understand that these multiple spikes (along the jet) or multiple bright dots (across the jet) are forming due to multiple enhancements in the intensity with time. Most probably, these multiple enhancements in the intensity support the multiple magnetic reconnection scenario (Morton et al. 2012; Li et al. 2015; Kumar et al. 2017). Spectroscopic observations reveal a periodic enhancement in the line width of Si IV 1393.77 Å (see Figures 6 and 7). For the first time, the periodic enhancement of the Si IV line width is reported in this blowout jet event. On top of these crucial observational findings, we notes that the Si IV profiles are blueshifted (upflows) when they are very broad (i.e., high line width) and, gradually, the profiles become narrower while they are moving toward the redshifts (downflows). The periodic existence of such broadened blueshifted Si IV profiles is most probably due to the occurrence of multiple magnetic reconnection in this blowout jet. Most importantly, our observations also reveal very complex and explosive types of profiles of some prominent spectral lines (Si IV, C II, and Mg II) of the solar interface region (see Figure 5). As we know that such complex and explosive types of profiles are produced only due to the magnetic reconnection (Peter et al. 2014; Innes et al. 2015; Huang et al. 2017; Young et al. 2018; Chitta & Lazarian 2020), all of the observational findings indicate the occurrence of multiple magnetic reconnection.

QPPs in the solar/stellar flares are often phenomena that occur within a few seconds to a few minutes of the oscillation period. Several reports discuss the triggering and related dynamics of QPPs in the solar atmosphere (e.g., Chen & Priest 2006; Inglis & Nakariakov 2009; Nakariakov & Melnikov 2009; Van Doorselaere et al. 2016; Li et al. 2017; Nakariakov et al. 2018; McLaughlin et al. 2018; Kashapova et al. 2020; Zhou et al. 2022; Shi et al. 2022). The statistical studies of the intense solar flares suggest that the occurrence rate of QPPs reaches 30%–80% with intense flares lying above the M5 class (Simões et al. 2015). However, the QPPs occurrence rates reduce with the low intensity solar flares

(Zimovets et al. 2021). Using Geostationary Operational Environmental Satellite (GOES) X-ray data from 2011 to 2018, Hayes et al. (2020) performed a statistical analysis for QPPs and their association with the different classes of solar flares. The authors claimed that  $\approx 46\%$  of X-class and  $\approx 29\%$  of M-class flares show QPP signatures. However, only  $\approx 9\%$  of C-class flares exhibit QPP signatures. On the other hand, there are few reported observations of QPPs in jets (Morton et al. 2012; Zhang & Ji 2014; Shen et al. 2018). Interestingly, in the present work, the wavelet analysis of light curves from five different boxes in various AIA filters clearly demonstrates the existence of QPPs in the present blowout jet (Section 3.6).

The triggering mechanisms of QPPs are very crucial, and so far, more than 15 mechanisms have been proposed to understand the initiation mechanisms of the QPPs (Nakariakov & Melnikov 2009; Van Doorselaere et al. 2016; Zimovets et al. 2021). Broadly, these triggering mechanisms of QPPs may be classified into two categories, namely, periodic spontaneous magnetic reconnection (Kliem et al. 2000; Karlický et al. 2005; Murray et al. 2009; Morton et al. 2012; Li et al. 2015; McLaughlin et al. 2018) and the MHD waves that may induce the periodic magnetic reconnection (e.g., Ning et al. 2004; Foullon et al. 2005; Nakariakov & Melnikov 2006; Nakariakov & Zimovets 2011; Kumar et al. 2016; Tian et al. 2016; Zhang et al. 2016; Zimovets et al. 2021). Ning et al. (2004) found recurring explosive events with a period of 3–5 minutes when the compressible waves push the oppositely directed field lines to reconnect. This process leads to multiple magnetic reconnection, and the QPPs were triggered by multiple magnetic reconnection (i.e., recurring explosive events). The other wave modes (e.g., fast mode MHD waves and global kink mode) may also trigger the periodic magnetic reconnection in a coronal loop that is situated near the flaring region. It initiates QPPs with a period of several minutes (e.g., Foullon et al. 2005; Nakariakov & Melnikov 2006). In the present work, the detected QPPs from various intensity light curves in the blowout jet have a period of  $\sim 3$  minutes (Section 3.6). The extracted EMs from the blowout jet in the temperature range of 0.5–15 MK also show the temporal variations on a timescale of  $\sim 3$  minutes (Section 3.4; Figure 4). Apart from the intensity and the EM curves, the line width of Si IV is also fluctuating on a timescale of approximately 3 minutes (Section 3.5). Hence, consistently, we found the fluctuations at a timescale of  $\sim 3$  minutes in various parameters (e.g., intensity, EMs, and line width). Here, we would like to mention that this blowout jet triggers within an active region (AR). The umbra of the sunspot (i.e., photospheric and chromospheric atmosphere of AR) is filled with the three-minute slow MHD waves (e.g., Fleck & Schmitz 1991; Botha et al. 2011; Jess et al. 2012; Tian et al. 2014; Chae et al. 2017; Felipe 2019; Farris & McAteer 2020; Felipe 2021; Kayshap et al. 2021b). Hence, we conjecture that three-minute oscillations are present within the triggering site of the blowout jet, and they may drive the periodic magnetic reconnection at timescale of  $\sim 3$  minutes. Hence, most probably, we can say that the periodic magnetic reconnection produces the QPPs in the intensity, EMs, and line width.

It should be noted that the magnetic reconnection between the preexisting and open coronal field and closed magnetic fields can produce a collimated jet without the rotation or twist, i.e., a kind of standard jet (Yokoyama & Shibata 1996; Miyagoshi & Yokoyama 2003; Moreno-Insertis et al. 2008;

Moore et al. 2010; Liu et al. 2011; Moreno-Insertis & Galsgaard 2013; Raouafi et al. 2016; Shen 2021). On the other hand, the magnetic reconnection between the preexisting open coronal magnetic field and the twisted, closed magnetic fields can produce newly twisted magnetic field lines which undergo the untwisting motions (e.g., Fang et al. 2014). The plasma flows along the newly twisted magnetic field lines that form the solar jet, and the rotational/helical motion of the solar jets is a result of the untwisting motion of these newly twisted magnetic field lines. Hence, magnetic reconnection is an important physical process to trigger the solar jets in the solar atmosphere (Shibata et al. 1992; Yokoyama & Shibata 1995; Shimojo et al. 1996, 1998; Shibata et al. 2007; Kayshap et al. 2013a, 2013b, 2018; Tian et al. 2014; Jelínek et al. 2015; Sterling et al. 2015; Wyper et al. 2017; Srivastava et al. 2021). That is why this physical process (magnetic reconnection) is an integral feature of various 2.5D and 3D models of the solar jets (Yokoyama & Shibata 1996; Moreno-Insertis et al. 2008; Nishizuka et al. 2008; Gontikakis et al. 2009; Pariat et al. 2015, 2016). The present blowout jet shows a very strong rotation of the plasma column (see Figure A1 animation). The helical or rotational motions of the solar jets are an important indication of kink instability (e.g., Shibata et al. 1996; Raouafi et al. 2016; Shen 2021). The numerical simulations show that destabilization of the system by global kink instability (when the helicity or twist exceeded the critical value) can trigger magnetic reconnection through the separatrix surface, and magnetic reconnection drives the helical solar jets (e.g., Pariat et al. 2009, 2010; Rachmeler et al. 2010; Pariat et al. 2015). Most of the magnetic field is either open or a long curvature magnetic field in the vicinity of the blowout jet (see panels (c1) and (d1) of Figure 2). Here, we mention that kink instability destabilizes the preexisting coronal magnetic field configuration through either magnetic reconnection between the kinked flux rope (i.e., kinked/erupting loops) and the preexisting coronal fields or the internal magnetic reconnection within the kink-unstable flux rope. Hence, due to the magnetic reconnection, the plasma flows along the reconnected magnetic field lines, which collectively form the spire of the blowout jet. This blowout jet is mainly visible in the cool temperature filters, and the signature of this blowout jet is faint in the hot temperature filters (see Section 3.2). However, usually, the blowout jets have strong emissions at hot temperatures along with strong emissions at cool temperatures (e.g., Moore et al. 2010, 2013). Here, it should be noted that surges emit mainly at cool temperatures. Therefore, in the present observational baseline, we do not rule out the possibility of this jet being an chromospheric surge. However, the EM in high-temperature wave bands also shows some hot plasma emission (4–6 MK) from the spire of this jet. Therefore, this paper uses this feature as a blowout jet.

Hence, kink instability is possibly an important driver of solar jets, and not only in the solar jets, but the kink instability also plays a crucial role in the triggering of the large-scale eruptions of the solar atmosphere (Török et al. 2004; Török & Kliem 2005; Srivastava et al. 2010; Kumar et al. 2012; Srivastava et al. 2013; Zhong et al. 2021). In cases of observations related to the kinked solar flux rope in the solar jets, Kayshap et al. (2013a) reported a kinked flux tube that drives a solar jet, i.e., internal magnetic

reconnection in the kinked flux tube at the north pole triggers the polar jet. Further, Zhu et al. (2017) have also shown that kink instability triggers a blowout jet in the solar atmosphere. The present observation clearly shows the occurrence of the kinked flux rope at the west limb prior to the jet formation. Further, the imaging, as well as spectroscopic observations, confirms multiple magnetic reconnections in support of the formation of this solar blowout jet.

Hence, in conclusion, we say that the present observational baseline shows the inverse  $\gamma$ -shaped, rotational or helical motion, and multiple magnetic reconnections in this blowout jet event. Most probably, these observational findings collectively indicate that the kink instability triggers this blowout jet, and multiple magnetic reconnections lead to the formation of QPPs in this jet.

S.K.M. acknowledges the Indian Institute of Astrophysics (IIA, Bangalore) for providing the computational facilities and institute fellowship. K.S. would like to acknowledge the Council of Scientific & Industrial Research (CSIR), Government of India, for financial support through a Senior Research Fellowship (UGC-SRF). P.J. acknowledges support from grant 21-16508J of the Grant Agency of the Czech Republic. A.K.S. acknowledges the ISRO Project Grant (DS\_2B-13012(2)/26/2022-Sec.2) for the support of his research. S.P.R. acknowledges support from SERB (Govt of India) research grant CRG/2019/003786. We acknowledge Hannah & Kontar (2012) for calculating the DEM. The data is courtesy of SDO/AIA and IRIS science team. We also acknowledge the use of the method of Torrence & Compo (1998) to extract the wavelet power spectra and the average period of QPPs.

## Appendix A

### Temporal Evolution of the Jet in the IRIS/SJI 1330 Å Filter

We have shown the evolution of the jet in IRIS/SJI 1330 Å filter observations (see Figure A1). At  $t = 06:29$  UT, we see the activation of the flux rope at the west limb of the Sun (panel (a)). Further, we see the formation of the bright knots that are most probably forming due to the magnetic reconnection (panel (d)), and this magnetic reconnection triggers the jet (panel (d)). Magnetic reconnection happens in the vicinity of the bright knots, therefore, below the bright knots the plasma falls back toward the limb (downflows) along both legs (indicated by the red arrows in panel (f)). While above the bright knot the plasma flows upward as indicated by the blue arrow in panel (f). Around  $t = 06:33$  UT, the northern leg of the jet erupts completely (panel (h)), and further, the jet evolves around the southern leg (panels (h) and (i)). In the later phase of the jet, we see that most of the plasma falls back toward the solar surface. The evolution and dynamics of the jet in this filter (i.e., IRIS/SJI 1330 Å) are very similar to what we already saw in the AIA 304 Å filter (see Figure 1). The dynamics and evolution of this jet with the help of the AIA 304 Å filter are discussed in the main text. Similar to the AIA 304 Å filter, we tracked a plasma thread that shows rotation with time (see the curved white arrows from panels (d) to (f)). A similar evolution of this jet can be seen in the given animations (Figure A1 animation with and without annotations). The real-time duration of the IRIS animation is 23 s. Here, it should be noted that the IRIS observations are rotated by a roll angle of  $90^\circ$ , and we provided the directional arrows in the first panel of Figure A1.

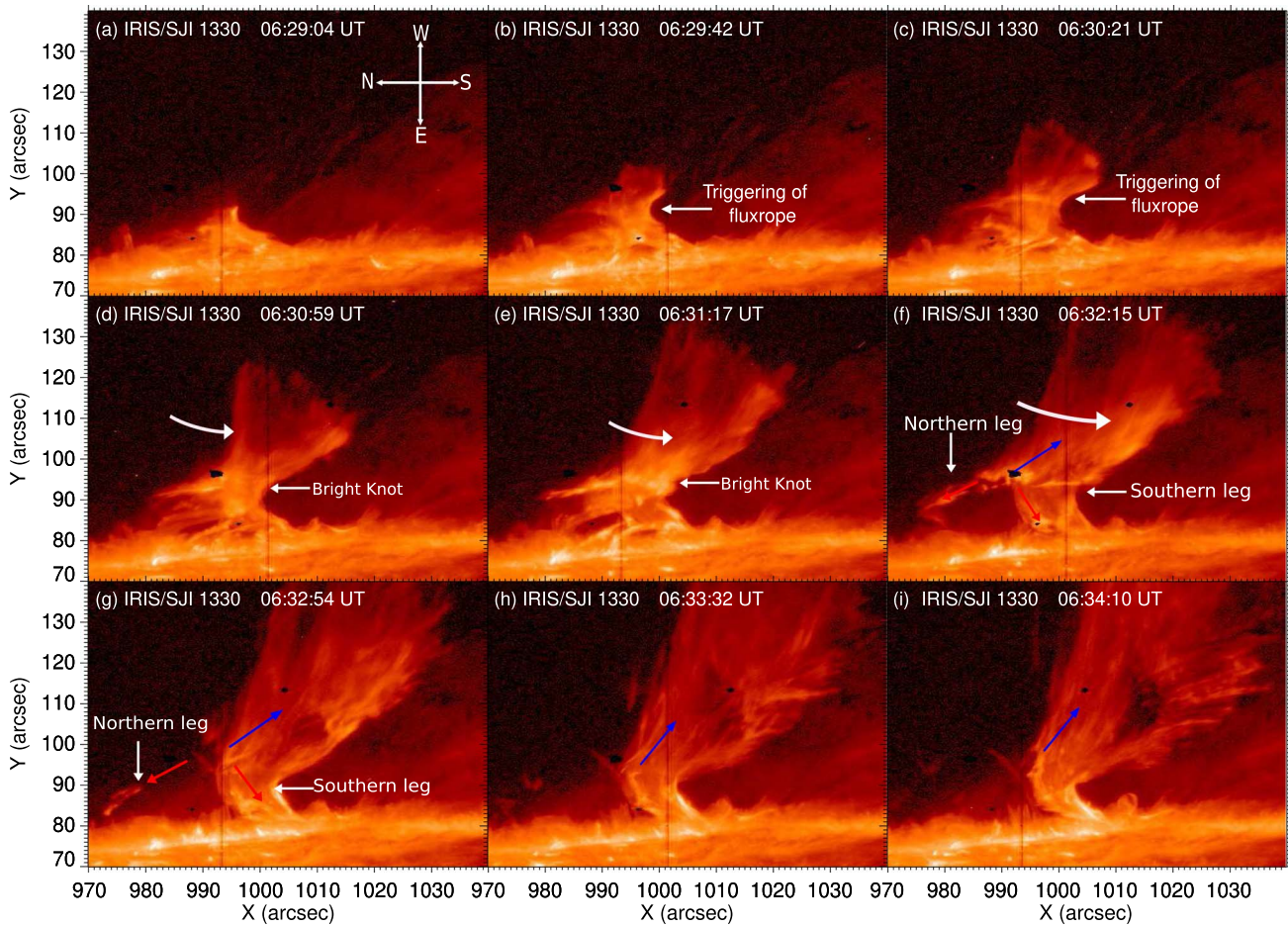


**Figure A1.** This figure shows the evolution of the jet in the IRIS/SJI 1330 Å filter. First, we saw the activation of the kinked flux rope (panels (b) and (c)), and then the formation of bright knots due to the magnetic reconnection of twisted field lines (panel d). This magnetic reconnection leads downflows along both legs of the jet (see the red arrows in panel (f)) and upflows along the spine of the jet (blue arrow in panel (f)). Further, after some time, one leg erupts completely (panels (g) and (h)), and the jet further develops along the southern leg (panels (h) and (i)). We also see the rotation of the plasma as indicated by the white arrows in panels (d) to panel (f). At last, we mention that the evolution of the jet in IRIS/SJI 1330 Å is similar to that of AIA 304 Å (see Figure 1). An animation of this figure showing the same evolution of this jet is available. The animation shows the same sequence with annotations (top panel) and without annotations (bottom panel). The IRIS animations start from 06:24:07 UT to 07:00:50 UT having a real-time duration of 23 s.

(An animation of this figure is available.)

### Appendix B Quasi-periodic Pulsations: AIA 171 Å, AIA 211 Å, and AIA 131 Å

In this appendix, we show the wavelet analysis for AIA 171 Å (Figure B1), AIA 131 Å (Figure B2), and AIA 211 Å

(Figure B3). We show the wavelet power maps from all four boxes in the same fashion as described in Section 3.6. Interestingly, the QPPs in these hot EUV wave bands of SDO/AIA also show a similar period as those we found for AIA 304 Å (Section 3.6).

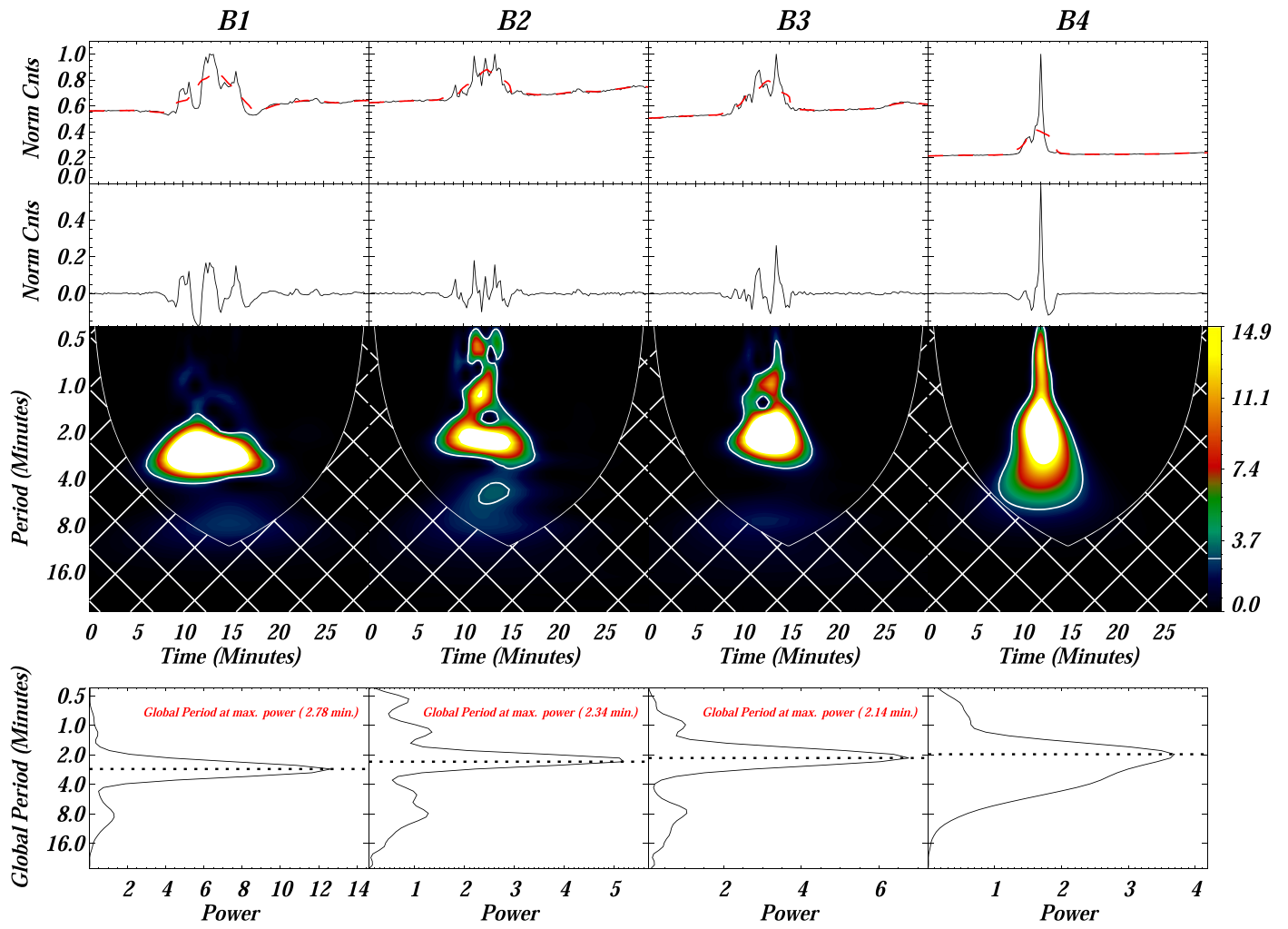


Figure B1. Same as Figure 8 but for AIA 171 Å filter observations.

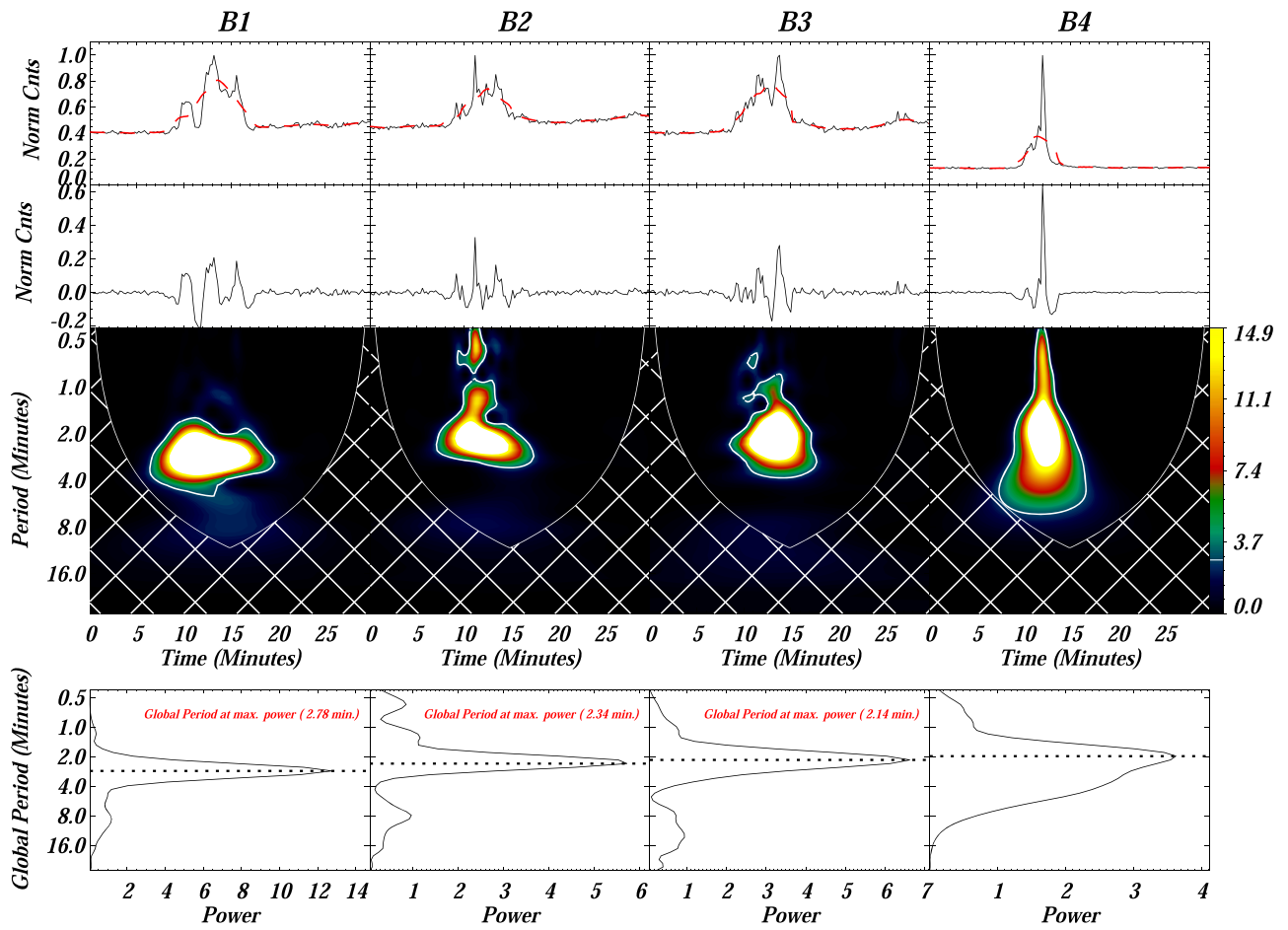


Figure B2. Same as Figure 8 but for AIA 131 Å filter observations.

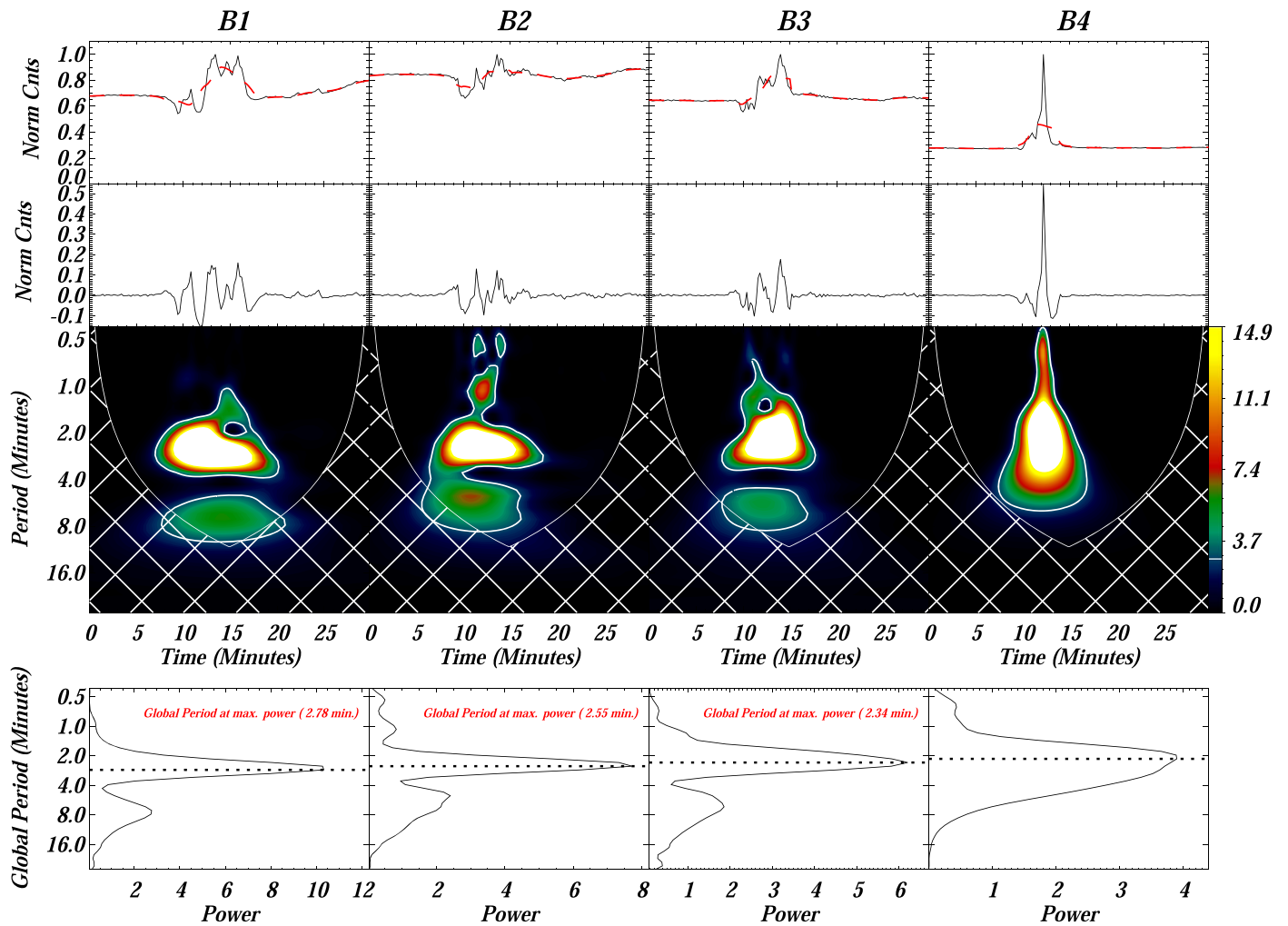


Figure B3. Same as Figure 8, but for the AIA 211 Å filter observations.

## ORCID iDs

Sudheer K. Mishra <https://orcid.org/0000-0003-2129-5728>  
 Kartika Sangal <https://orcid.org/0000-0003-0596-5277>  
 Pradeep Kayshap <https://orcid.org/0000-0002-1509-3970>  
 Petr Jelínek <https://orcid.org/0000-0002-7208-8342>  
 S. P. Rajaguru <https://orcid.org/0000-0003-0003-4561>

## References

- Antolin, P., Pagano, P., Testa, P., Petralia, A., & Reale, F. 2021, *NatAs*, 5, 54  
 Archontis, V., & Hood, A. W. 2013, *ApJL*, 769, L21  
 Aschwanden, M. J. 2004, *Physics of the Solar Corona. An Introduction* (Chichester: Praxis Publishing Ltd.)  
 Bahauddin, S. M., Bradshaw, S. J., & Winebarger, A. R. 2021, *NatAs*, 5, 237  
 Botha, G. J. J., Arber, T. D., Nakariakov, V. M., & Zhugzhda, Y. D. 2011, *ApJ*, 728, 84  
 Canfield, R. C., Reardon, K. P., Leka, K. D., et al. 1996, *ApJ*, 464, 1016  
 Chae, J., Lee, J., Cho, K., et al. 2017, *ApJ*, 836, 18  
 Chen, P. F., & Priest, E. R. 2006, *SoPh*, 238, 313  
 Chitta, L. P., & Lazarian, A. 2020, *ApJL*, 890, L2  
 Cirtain, J. W., Golub, L., Lundquist, L., et al. 2007, *Sci*, 318, 1580  
 De Pontieu, B., Polito, V., Hansteen, V., et al. 2021, *SoPh*, 296, 84  
 De Pontieu, B., Title, A. M., Lemen, J. R., et al. 2014, *SoPh*, 289, 2733  
 Fang, F., Fan, Y., & McIntosh, S. W. 2014, *ApJL*, 789, L19  
 Farris, L., & McAteer, R. T. J. 2020, *ApJ*, 903, 19  
 Felipe, T. 2019, *A&A*, 627, A169  
 Filippov, B., Srivastava, A. K., Dwivedi, B. N., et al. 2015, *MNRAS*, 451, 1117  
 Fleck, B., & Schmitz, F. 1991, *A&A*, 250, 235  
 Felipe, T. 2021, *NatAs*, 5, 2  
 Foullon, C., Verwichte, E., Nakariakov, V. M., & Fletcher, L. 2005, *A&A*, 440, L59  
 Gontikakis, C., Archontis, V., & Tsinganos, K. 2009, *A&A*, 506, L45  
 Hayes, L. A., Inglis, A. R., Christe, S., Dennis, B., & Gallagher, P. T. 2020, *ApJ*, 895, 50  
 Hassanin, A., & Kliem, B. 2016, *ApJ*, 832, 106  
 Hannah, I. G., & Kontar, E. P. 2012, *A&A*, 539, A146  
 Harrison, R. A., Bryans, P., & Bingham, R. 2001, *A&A*, 379, 324  
 Hood, A. W., & Priest, E. R. 1981, *GApFD*, 17, 297  
 Hong, J.-C., Jiang, Y.-C., Yang, J.-Y., et al. 2013, *RAA*, 13, 253  
 Huang, Z., Madjarska, M. S., Scullion, E. M., et al. 2017, *MNRAS*, 464, 1753  
 Huang, Z., Madjarska, M. S., Xia, L., et al. 2014, *ApJ*, 797, 88  
 Inglis, A. R., & Nakariakov, V. M. 2009, *A&A*, 493, 259  
 Innes, D. E., Guo, L.-J., Huang, Y.-M., & Bhattacharjee, A. 2015, *ApJ*, 813, 86  
 Innes, D. E., Inhester, B., Axford, W. I., et al. 1997, *Natur*, 386, 811  
 Jess, D. B., De Moortel, I., Mathioudakis, M., et al. 2012, *ApJ*, 757, 160  
 Jelínek, P., Srivastava, A. K., Murawski, K., Kayshap, P., & Dwivedi, B. N. 2015, *A&A*, 581, A131  
 Jibben, P., & Canfield, R. C. 2004, *ApJ*, 610, 1129  
 Karlický, M., Bárta, M., Mészárosová, H., & Zlobec, P. 2005, *A&A*, 432, 705  
 Kamio, S., Curdt, W., Teriaca, L., Inhester, B., & Solanki, S. K. 2010, *A&A*, 510, L1  
 Kashapova, L. K., Kupriyanova, E. G., Xu, Z., Reid, H. A. S., & Kolotkov, D. Y. 2020, *A&A*, 642, A195  
 Kayshap, P., Murawski, K., Srivastava, A. K., & Dwivedi, B. N. 2018, *A&A*, 616, A99  
 Kayshap, P., Srivastava, A. K., Murawski, K., & Tripathi, D. 2013a, *ApJL*, 770, L3  
 Kayshap, P., Srivastava, A. K., & Murawski, K. 2013b, *ApJ*, 763, 24

- Kayshap, P., Singh Payal, R., Tripathi, S. C., & Padhy, H. 2021a, *MNRAS*, **505**, 5311
- Kayshap, P., Tripathi, D., & Jelínek, P. 2021b, *ApJ*, **906**, 121
- Kliem, B., Karlický, M., & Benz, A. O. 2000, *A&A*, **360**, 715
- Kumar, P., Cho, K.-S., Bong, S.-C., Park, S.-H., & Kim, Y. H. 2012, *ApJ*, **746**, 67
- Kumar, P., Nakariakov, V. M., & Cho, K.-S. 2016, *ApJ*, **822**, 7
- Kumar, P., Nakariakov, V. M., & Cho, K.-S. 2017, *ApJ*, **836**, 121
- Kruskal, M. D., & Kulsrud, R. M. 1958, *PhFl*, **1**, 265
- Lemen, J. R., Title, A. M., Akin, D. J., et al. 2012, *SoPh*, **275**, 17
- Li, D., Ning, Z. J., & Zhang, Q. M. 2015, *ApJ*, **807**, 72
- Li, D., Zhang, Q. M., Huang, Y., Ning, Z. J., & Su, Y. N. 2017, *A&A*, **597**, L4
- Liu, J., Wang, Y., & Erdélyi, R. 2019, *FrASS*, **6**, 44
- Liu, C., Deng, N., Liu, R., et al. 2011, *ApJL*, **735**, L18
- Matsui, Y., Yokoyama, T., Kitagawa, N., & Imada, S. 2012, *ApJ*, **759**, 15
- McLaughlin, J. A., Nakariakov, V. M., Dominique, M., Jelinek, P., & Takasao, S. 2018, *SSRv*, **214**, 45
- Mishra, S. K., Singh, T., Kayshap, P., & Srivastava, A. K. 2018, *ApJ*, **856**, 86
- Mishra, S. K., & Srivastava, A. K. 2019, *ApJ*, **874**, 57
- Mishra, S. K., Singh, B., Srivastava, A. K., Kayshap, P., & Dwivedi, B. N. 2021, *ApJ*, **923**, 72
- Miyagoshi, T., & Yokoyama, T. 2003, *ApJL*, **593**, L133
- Moreno-Insertis, F., Galsgaard, K., & Ugarte-Urra, I. 2008, *ApJL*, **673**, L211
- Moreno-Insertis, F., & Galsgaard, K. 2013, *ApJ*, **771**, 20
- Moore, R. L., Cirtain, J. W., Sterling, A. C., & Falconer, D. A. 2010, *ApJ*, **720**, 757
- Moore, R. L., Sterling, A. C., Falconer, D. A., & Robe, D. 2013, *ApJ*, **769**, 134
- Morton, R. J., Srivastava, A. K., & Erdélyi, R. 2012, *A&A*, **542**, A70
- Mulay, S. M., Zanna, G. D., & Mason, H. 2017, *A&A*, **598**, A11
- Murray, M. J., van Driel-Gesztelyi, L., & Baker, D. 2009, *A&A*, **494**, 329
- Nakariakov, V. M., Anfinogentov, S., Storozhenko, A. A., et al. 2018, *ApJ*, **859**, 154
- Nakariakov, V. M., & Melnikov, V. F. 2006, *A&A*, **446**, 1151
- Nakariakov, V. M., & Melnikov, V. F. 2009, *SSRv*, **149**, 119
- Nakariakov, V. M., Inglis, A. R., Zimovets, I. V., et al. 2010, *PPCF*, **52**, 124009
- Nakariakov, V. M., Piliipenko, V., Heilig, B., et al. 2016, *SSRv*, **200**, 75
- Nakariakov, V. M., & Zimovets, I. V. 2011, *ApJL*, **730**, L27
- Ni, L., Zhang, Q.-M., Murphy, N. A., & Lin, J. 2017, *ApJ*, **841**, 27
- Ning, Z., Innes, D. E., & Solanki, S. K. 2004, *A&A*, **419**, 1141
- Nishizuka, N., Shimizu, M., Nakamura, T., et al. 2008, *ApJL*, **683**, L83
- Nóbrega-Siverio, D., Martínez-Sykora, J., Moreno-Insertis, F., et al. 2017, *ApJ*, **850**, 153
- Nóbrega-Siverio, D., Moreno-Insertis, F., & Martínez-Sykora, J. 2018, *ApJ*, **858**, 8
- Nóbrega-Siverio, D., Moreno-Insertis, F., & Martínez-Sykora, J. 2016, *ApJ*, **822**, 18
- Pariat, E., Antiochos, S. K., & DeVore, C. R. 2009, *ApJ*, **691**, 61
- Pariat, E., Antiochos, S. K., & DeVore, C. R. 2010, *ApJ*, **714**, 1762
- Pariat, E., Dalmasse, K., DeVore, C. R., Antiochos, S. K., & Karpen, J. T. 2016, *A&A*, **596**, A36
- Pariat, E., Dalmasse, K., DeVore, C. R., Antiochos, S. K., & Karpen, J. T. 2015, *A&A*, **573**, A130
- Peter, H., Tian, H., Curdt, W., et al. 2014, *Sci*, **346**, 1255726
- Rachmeler, L. A., Pariat, E., DeForest, C. E., Antiochos, S., & Torok, T. 2010, *ApJ*, **715**, 1556
- Raouafi, N.-E., Georgoulis, M. K., Rust, D. M., & Bernasconi, P. N. 2010, *ApJ*, **718**, 981
- Raouafi, N. E., Patsourakos, S., Pariat, E., et al. 2016, *SSRv*, **201**, 1
- Schmieder, B., Shibata, K., Van Driel-Gesztelyi, L., & Freeland, S. 1995, *SoPh*, **156**, 245
- Shen, Y., Liu, Y. D., Su, J., Qu, Z., & Tian, Z. 2017, *ApJ*, **851**, 67
- Shen, Y., Tang, Z., Li, H., & Liu, Y. 2018, *MNRAS*, **480**, L63
- Shen, Y. 2021, *RSPSA*, **477**, 20200217
- Shi, F., Li, D., & Ning, Z. 2022, *Univ*, **8**, 104
- Shibata, K., & Uchida, Y. 1986, *SoPh*, **103**, 299
- Shibata, K., Ishido, Y., Acton, L. W., et al. 1992, *PASJ*, **44**, L173
- Shibata, K., Yokoyama, T., & Shimojo, M. 1996, *AdSpR*, **17**, 197
- Shibata, K., Nakamura, T., Matsumoto, T., et al. 2007, *Sci*, **318**, 1591
- Shimojo, M., Hashimoto, S., Shibata, K., et al. 1996, *PASJ*, **48**, 123
- Shimojo, M., Shibata, K., & Harvey, K. L. 1998, *SoPh*, **178**, 379
- Shimojo, M., Shibata, K., Yokoyama, T., & Hori, K. 2001, *ApJ*, **550**, 1051
- Simões, P. J. A., Hudson, H. S., & Fletcher, L. 2015, *SoPh*, **290**, 3625
- Srivastava, A. K., Erdélyi, R., Tripathi, D., et al. 2013, *ApJL*, **765**, L42
- Srivastava, A. K., Mishra, S. K., & Jelínek, P. 2021, *ApJ*, **920**, 18
- Srivastava, A. K., & Murawski, K. 2011, *A&A*, **534**, A62
- Srivastava, A. K., Murawski, K., Kuźma, B., et al. 2018, *NatAs*, **2**, 951
- Srivastava, A. K., Zaqarashvili, T. V., Kumar, P., & Khodachenko, M. L. 2010, *ApJ*, **715**, 292
- Sterling, A. C. 2000, *SoPh*, **196**, 79
- Sterling, A. C., Chifor, C., Mason, H. E., Moore, R. L., & Young, P. R. 2010, *A&A*, **521**, A49
- Sterling, A. C., Moore, R. L., Falconer, D. A., & Adams, M. 2015, *Natur*, **523**, 437
- Tian, H., DeLuca, E. E., Cranmer, S. R., et al. 2014, *Sci*, **346**, 1255711
- Tian, H., DeLuca, E., Reeves, K. K., et al. 2014, *ApJ*, **786**, 137
- Tian, H., Young, P. R., Reeves, K. K., et al. 2016, *ApJL*, **823**, L16
- Tiwari, S. K., Moore, R. L., Winebarger, A. R., & Alpert, S. E. 2016, *ApJ*, **816**, 92
- Torrence, C., & Compo, G. P. 1998, *BAMS*, **79**, 61
- Török, T., Berger, M. A., & Kliem, B. 2010, *A&A*, **516**, A49
- Török, T., & Kliem, B. 2005, *ApJL*, **630**, L97
- Török, T., Kliem, B., Berger, M. A., et al. 2014, *PPCF*, **56**, 064012
- Török, T., Kliem, B., & Titov, V. S. 2004, *A&A*, **413**, L27
- Tziotziou, K., Tsiropoula, G., & Sutterlin, P. 2005, *A&A*, **444**, 265
- Van Doorselaere, T., Kupriyanova, E. G., & Yuan, D. 2016, *SoPh*, **291**, 3143
- Wyper, P. F., Antiochos, S. K., & DeVore, C. R. 2017, *Natur*, **544**, 452
- Wyper, P. F., DeVore, C. R., & Antiochos, S. K. 2018, *ApJ*, **852**, 98
- Yang, S., Zhang, Q., Xu, Z., et al. 2020, *ApJ*, **898**, 101
- Young, P. R. 2015, *ApJ*, **801**, 124
- Young, P. R., Keenan, F. P., Milligan, R. O., & Peter, H. 2018, *ApJ*, **857**, 5
- Yokoyama, T., & Shibata, K. 1995, *Natur*, **375**, 42
- Yokoyama, T., & Shibata, K. 1996, *PASJ*, **48**, 353
- Zaqarashvili, T. V., Lomineishvili, S., Leitner, P., et al. 2021, *A&A*, **649**, A179
- Zhang, Q. M., & Ji, H. S. 2014, *A&A*, **561**, A134
- Zhang, Q. M., & Ji, H. S. 2014, *A&A*, **567**, A11
- Zhang, Q. M., Li, D., & Ning, Z. J. 2016, *ApJ*, **832**, 65
- Zhang, Q. M., & Ni, L. 2019, *ApJ*, **870**, 113
- Zhelyazkov, I. 2012, *A&A*, **537**, A124
- Zhou, X., Shen, Y., Liu, Y. D., et al. 2022, *ApJL*, **930**, L5
- Zhong, Z., Guo, Y., & Ding, M. D. 2021, *NatCo*, **12**, 2734
- Zhu, X., Wang, H., Cheng, X., & Huang, C. 2017, *ApJL*, **844**, L20
- Zimovets, I. V., McLaughlin, J. A., Srivastava, A. K., et al. 2021, *SSRv*, **217**, 66